



**GEOLOGICAL SURVEY OF CANADA  
OPEN FILE 6988**

**Southampton Island Magnetotelluric Survey: Data Acquisition and  
Preliminary Analysis**

**J.E. Spratt, J.A. Craven and M. Sanborn-Barrie**

**2012**



Natural Resources  
Canada

Ressources naturelles  
Canada

**Canada**



**GEOLOGICAL SURVEY OF CANADA  
OPEN FILE 6988**

**Southampton Island magnetotelluric survey: data acquisition and  
preliminary analysis**

**Spratt, J.E.<sup>1</sup>, Craven, J.A.<sup>2</sup> and Sanborn-Barrie, M.<sup>2</sup>**

<sup>1</sup>Magnetotelluric Consultant, Wakefield, QC

<sup>2</sup>Geological Survey of Canada, Ottawa, ON

**2012**

©Her Majesty the Queen in Right of Canada 2012

doi:10.4095/291384

This publication is available from the Geological Survey of Canada Bookstore  
([http://gsc.nrcan.gc.ca/bookstore\\_e.php](http://gsc.nrcan.gc.ca/bookstore_e.php)).

It can also be downloaded free of charge from GeoPub (<http://geopub.nrcan.gc.ca/>).

**Recommended citation**

Spratt, J.E., Craven, J.A., and Sanborn-Barrie, M., 2012. Southampton Island magnetotelluric survey: data acquisition and preliminary analysis; Geological Survey of Canada Open File 6988, 39 p. doi:10.4095/29138

Publications in this series have not been edited; they are released as submitted by the authors.

## Table of Contents

Table of Contents .....	iii
Introduction.....	1
Data Acquisition and Processing.....	1
Decomposition Analysis .....	3
Depth Estimates .....	5
Ocean Effects .....	5
Data Modeling.....	6
1-D Models .....	6
2-D Models .....	7
Preliminary Interpretation and Discussion.....	8
Conclusions.....	9
References.....	10
Figure Captions.....	11

## **Introduction**

The Southampton Island Integrated Geoscience project was launched in 2007 as a joint initiative between the Canada-Nunavut Geoscience Office and the Geological Survey of Canada to update geoscience knowledge and allow the island's mineral and energy resource potential to be assessed in a modern context. At the start of the project, available gravity (Goodacre et al. 1987) and newly acquired aeromagnetic data (Coyle, 2008; deBeers pers comm. 2008) highlighted a profound discordance in geophysical trends between the eastern half of the island that exposes Precambrian rocks, and its southwest part which is overlain by Paleozoic cover. Accordingly, broadband and long period magnetotelluric data were acquired along profiles targeted to contribute an understanding of the deep lithosphere beneath Southampton Island and to investigate the potential presence of a crustal-scale feature (e.g. terrane boundary) underlying this region. In addition to providing insight into crustal architecture in the vicinity of Southampton Island, these MT data will enhance and complement interpretations of MT data along other transects of Nunavut (Figure 1), collected as part of the GEM (Geomapping of Energy and Minerals) program. These transects are designed to study the deep lithosphere beneath the Slave and Churchill provinces of northern Canada to better understand the potential for diamonds and reduce exploration risks. Collectively, they constitute a substantial dataset from which a regional 3-dimensional conductivity model and localized 2-D models will be generated.

This paper presents a preliminary analysis of the Southampton Island MT data, utilizing modern, robust, remote-referencing methods in a study of dimensionality, effects of distortion, and geoelectric strike angles. These preliminary results will be used to refine more sophisticated follow-up modelling.

## **Data Acquisition and Processing**

Both broadband (BBMT) and long period magnetotelluric (LMT) data was acquired over Southampton Island in 2007 and 2008. BBMT data were collected using Phoenix Geophysics recording instruments and sensors at 29 sites, located in 3 main areas (Figure 2): along a 120 km profile (profile A) that extends from Paleozoic sedimentary cover in the southwest to exposed Precambrian basement to the northeast; along a parallel, 50 km northeast-trending profile (profile B) situated wholly on Paleozoic sedimentary rock; and as a 3-station array perpendicular to the north end of profile A. The electric fields were measured in the two horizontal perpendicular directions using lead-lead chloride porous pots, and the magnetic fields were recorded in two horizontal directions and, where

possible, the vertical direction. In the summer of 2007, BBMT data were collected at 12 sites, where the magnetic field components were recorded using three separate MTC50 Phoenix coils that were mounted on tripods for orientation and stabilization. Recording time for these sites ranged from 1 to 20 hours (Table 1). In the summer of 2008, an additional 17 BBMT sites were acquired with the horizontal coils dug into the earth, and the vertical fields recorded at some locations with an air loop secured in place with rocks. For these sites, recording times ranged between 32 and 69 hours (Table 1). The BBMT data were processed from time series to response functions (apparent resistivity and phase curves) using robust remote reference techniques (Method 6 in Jones et al., 1989), as implemented by the Phoenix Geophysics software package MT2000, and yielded apparent resistivity and phase response curves in the period range of 0.004 s up to 1,000 s for most sites along both profiles (e.g., Figure 3a). The data quality is highly variable with some sites showing large error bars and large scatter in the response curves. Two sites with recording times <4 hours (sites sig011 and sig012) produced data of extremely poor quality which has been excluded from subsequent analysis. It is believed that wind noise on the tripod and shorter recording times in 2007, in general, resulted in lower quality data than that obtained in 2008 (see Appendix A).

In the summer of 2008, long period magnetotelluric (LMT) data were collected at 6 sites, most located on exposed Precambrian intrusive and metamorphic rocks, using the LiMS (Long Period Intelligent Magnetotelluric System) recording instrumentation (Figure 2). The electrical fields were recorded in two horizontal, perpendicular directions using lead-lead-chloride porous pots, while the magnetic fields were recorded in two horizontal directions and one vertical direction using a 3-component fluxgate magnetometer. Data were acquired for 4 – 14 days with little interruptions in the data acquisition (Table 1). The LMT data were processed using the multi-remote-reference, robust, cascade decimation code of Jones and Jödicke (1984), generating apparent resistivity and phase response curves as a function of period for each site. In general, the data quality is reasonable with smooth response curves and low error bars from 10 s up to 10,000 s (e.g., Figure 3b). Both BBMT and LMT data were collected at site sig202. The resulting response curves were merged together to generate response curves with a period range of 0.004 – 10,000 s, spanning nearly 8 decades (Figure 3c).

Several of the sites show out-of-quadrant phase responses, where the phase of one or both modes goes above 90° or drops below 0° (Figure 3d). This is a possible indication of either current channeling, near-surface anisotropy or 3-dimensional distortion. Out-of-quadrant phase responses are often observed where there is a high contrast in near-surface conductivity values, such as recording data in a sediment-filled valley between large resistive mountains, or at sites located directly on

conductive dykes or faults. It is not possible, at the periods where the phases are out of quadrant for a 2-dimensional structure to accurately reproduce the data. Accordingly, these sites will be excluded from generation of 2-D models of the subsurface. Several of these sites are located on Paleozoic strata at the southwest end of the survey area, a region transected by a series of northwest-trending faults that may have contributed to this distortion (Figure 4).

## **Decomposition Analysis**

Data from each site were analyzed using Groom-Bailey decomposition techniques to understand the degree of dimensionality, determine the most appropriate geoelectric strike direction where the data are 2-dimensional, and remove the effects of galvanic distortion in the data (Groom and Bailey, 1989). Single site decompositions were applied to each site using the method described in McNeice and Jones (2001). Where the phase difference between the TE- and TM-modes is minimal ( $<10^\circ$ ), the data can be considered 1-dimensional, or independent of the geoelectrical strike angle. Where the phase difference is larger, the data are more dependent on the strike angle, and 2-D models need to be generated at the appropriate geoelectric strike angle in order to accurately represent the subsurface conductivity structure. At short periods, where the fields are penetrating the top few kilometers, the geoelectric strike usually follows geologic trends and these trends can be used to resolve the  $90^\circ$  strike ambiguity inherent in the analysis. Ideally, a model is generated along a profile at one strike angle for all periods. However, where the subsurface structure is complex, this strike angle may change along profile or with depth, such that the profile may need to be divided into sections and modelled separately at the appropriate geoelectric strike angles. In some cases, no strike angle can be found that fits the data within reasonable statistical limits (i.e., with a root-mean-square (RMS) misfit of  $< 3$ ) even when no constraints are placed on the period bandwidth. This is the case at some sites (SIG008, SIG110, SIG112) where, along with large RMS values, the data show highly variable twist or shear values that are indicators of galvanic distortion (Figure 5). The decomposition analysis suggests that the data may not be accurately represented with a 2-D model and a portion of the data at these sites may need to be omitted.

The strike directions resulting from single site, single decade period band decompositions with a  $90^\circ$  ambiguity and an error floor set to 3.5%, equivalent to  $2^\circ$  phase, are shown in figure 6. In general, below 0.01 s most sites show low phase differences (Fig. 6a), suggesting that the data are approximately 1-D. In a few exceptions, the phase difference is higher (i.e., SIG101, SIG103) and

these show a large scatter in the geoelectric strike angle indicating that localized structures are influencing the data. At periods between 0.01 and 10 s, there is a fairly consistent preferred strike angle of  $\sim 33^\circ$  (orthogonal direction to  $-57^\circ$ , see Fig 6c inset) for most of the BBMT sites, regardless of the phase difference (Fig 6a,b,c,d). At periods between 10 and 100 s, the BBMT data continue to show a preference of  $33^\circ$  (Fig. 6e), with the exception of a few sites at the center of profile A. This area corresponds to the location of sites with out-of-quadrant phases or high RMS values and is likely a result of local distortion. The LMT sites, where the phase differences are greatest show a strike preference of roughly  $45^\circ$  (Fig. 6e inset). At the longest periods (100 - 1000 s; Fig. 6f), phase differences are highest and more variable, and there is more scatter in the strike angle with geoelectric strikes as low as  $16^\circ$  ( $-74^\circ$ ). Collectively, this suggests poor data quality at these periods.

The extensive Paleozoic sediment cover obscures the geological relationships that are the preferred indicators to correct the  $90^\circ$  ambiguity in the geo-electric strike analysis. Publically available aeromagnetic coverage of the central part of Southampton Island shows some linearity reflected by near-surface geology which is mostly oblique to the preferred strike angles observed in the decomposition analysis (Figure 7), with the exception of the northernmost LMT sites at periods of 10 - 100 s. The aeromagnetic tilt data suggests that the strike for these LMT sites corresponds to the transverse electric mode (TE-mode) at  $45^\circ$  (parallel to strike) and the transverse magnetic mode (TM-mode) at  $-45^\circ$  (perpendicular to strike). In contrast, regional gravity data (Figure 8) and industry-acquired aeromagnetic data (deBeers pers comm 2008) highlight northwest-trending structures at the southwest ends of profiles A and B (Figure 8). This indicates that the TE-mode in the southwest is at a geoelectric strike angle of  $-57^\circ$  with the TM-mode at  $33^\circ$ .

Given the variable indications of TE-mode and the necessary condition for 2-D model studies of a uniform direction, the data have been recalculated at strike angles of  $33^\circ$ ,  $45^\circ$  and  $16^\circ$  to investigate the strike dependency of the responses. Figure 9 shows the misfit values for the whole period range along profile A. Where the misfit value is  $< \sim 2$ , a 2-D model can be generated to adequately represent the data. The geoelectric strike angle that best fits most of the sites over most of the period ranges is  $33^\circ$  (or  $-57^\circ$ ), however, several of the sites (i.e., SIG110, SIG104) at particular frequencies do not fit the data regardless of the strike angle selected. This is consistent with the results of single site, single frequency decomposition analysis. The misfit values for the whole period range along profile B are shown for strikes of  $16^\circ$ ,  $33^\circ$ , and  $45^\circ$  (Figure 10). Similar to profile A, the geoelectric strike angle that best fits most of the sites over most of the period range is  $33^\circ$  with the exception of site sig112 and sig116. Site sig112 showed high RMS values and strong twist and shear variations at periods greater between 1-10 s in the decomposition analysis, indicating that these data will not fit at any strike angle

at these periods (Fig. 5c). Site sig116 showed a preferred strike angle of  $\sim 2^\circ$  at periods below 0.1 s (*see* Fig. 6b) inconsistent with surrounding sites and likely due to localized 2-D structure. The misfit values for the remaining BBMT and LMT sites are shown for the same three strike angles in Figure 11. The RMS values are independent of the strike angle, suggesting that the data are predominantly 1-D.

Two-dimensional models generated along profile A and profile B were carried out using data recalculated at a strike angle of  $-57^\circ$  both with, and without, the misfitting data in order to assess how these sites affect the conductivity structure and the misfit value of the models to the data.

## Depth Estimates

Rough estimates of penetration depths were determined using Schmucker's c-function analysis which calculates the depth of maximum eddy current flow (Schmucker, 1970). These show that data penetration is much greater ( $>200$  km) at sites located on Precambrian basement (Figure 12). Within the Paleozoic succession, the Red Head Rapids Formation is known to host organic-rich shale intervals (Zhang, 2008) that commonly have resistivity values on the order of 10 ohm-m. These low resistivities can cause attenuation of the electric and magnetic fields, inhibiting penetration into the deep earth. In general, sites located on Paleozoic cover have sufficient penetration to image the crust and uppermost mantle structure, whereas sites located on exposed Precambrian crust are more likely to image the base of the lithosphere.

## Ocean Effects

It is known that the presence of sea water, a near-surface 3-dimensional conductive body, can have significant effects on MT data, due to the sharp contrast in resistivity between the land and the ocean (Schmucker, 1970, Menveillie et al., 1982). Coastal effects are typically observed in long period data and the severity of these effects is dependent on the salinity of the sea water, the conductivity structure of the subsurface, the depth of the ocean, and the proximity of the MT site to the coast (e.g. Jones, 1981, Santos et al., 2001, Pous et al., 2003). In order to assess the coastal effects on this data set, a 3-D mesh was created with ocean resistivity values of 0.3 ohm-m extending to depths of 500m, (approximated from the International Bathymetric Chart of the Arctic Ocean:

<http://www.ngdc.noaa.gov/mgg/bathymetry/arctic/arctic.html>), and uniform land resistivity values of 500 ohm-m (Figure 13). A forward inversion then generated synthetic response curves at the recorded site locations. This method of determining coastal effects is an approximation, as the coast line is not



exact, the depth and resistivity of the ocean is approximated, and a uniformly resistive earth was used rather than a more realistic layered or structured earth. The method does, however, highlight those sites where caution should be used in interpreting 2-dimensional models that include long period data.

The calculated forward response curves show that there is little seawater effect on data acquired along profile A, where the apparent resistivity and phases are consistent with a uniform half space of 500 ohm•m to periods of nearly 100 s (Figure 13). Moderate seawater effects are observed at periods as short as 10 s for sites along profile B. Depth analysis, similar to that described above, for site sig117 shows that 10 s corresponds to a depth of 17 km in the xy-mode and 35 km in the yx-mode, suggesting that these sites should be able to accurately image most of the crust. Depth analysis of site sig202 shows that 100 s in the XY mode corresponds to depths of 94 km suggesting that a conductivity model of crust and upper mantle should be relatively unaffected by the ocean. The strongest seawater effect is apparent at sig205 and sig204, at periods as early as 1s. This implies that the LMT data acquired from these two sites may have been disturbed by coastal effects throughout the entire recorded period range.

## Data Modeling

The distortion-corrected, regional 2-D responses from sites along profile A were imported in the WinGlink MT interpretation software package at a geoelectric strike angle of 33° (-57°) and 45°(-45°). These data were manually edited to remove data points with large error bars or large scatter, or data with phases above 90° or below 0°. The degree of static shift, arising from a charge buildup at the base of near-surface conductors, cannot be numerically determined; however, typically the effect is to raise the apparent resistivity values of the entire response curve. Where one apparent resistivity curve was much higher than another, the curve was dropped to match that of the other curve at the shortest period. This helps to reduce the effect of anisotropic shift, but does not account for the static-shift cases where both curves are affected.

## 1-D Models

One-dimensional layered earth models were generated for each site using Occam's inversion codes as implemented by the WinGlink MT interpretation software package and stitched together to create cross-sections along the Southampton MT profiles A (Fig. 14a) and B (Fig. 15a). Pseudosections of the phase responses for each of the sites along the profiles were generated for both the TE- and TM-modes (Figures 14b and 15b). As previously described in the phase difference plots, where these

sections are similar, the 1-D models can be considered to be a valid representation of the Earth, notwithstanding static shift effects. Few similarities are observed between the TE- and TM-modes in the 1-D models or the phase pseudosections along profiles A and B. This is a strong indication that the data are structurally complex, requiring 2-D or 3-D modelling to image the subsurface. 1-D models of the TM- and TE-modes were also generated for the remaining BBMT sites and the LMT sites (Figure 16). With the exception of site sig206, 1-D models for the two modes show strong similarities suggesting that the subsurface away from profiles A and B is laterally uniform.

## 2-D Models

As is common with many regularized inversion codes, the 2-D code used searches iteratively for the smoothest model that best fits the data by attempting to trade off the fit to the observed data (data misfit) with the squared Laplacian (smoothing term) of the horizontal and vertical resistivity gradients. The inversion program searches for the smoothest, best-fit model with the least deviation from the starting model, which is usually a half space (Mackie and Madden, 1993). This means that the derived 2-D models represent the minimum structure required to fit the data with an acceptable misfit.

Many different models need to be generated using various combinations of modes and parameters in order to observe the effects of these changes on the model structure and to derive the most robust final model with an appropriate misfit value. Several models were generated from the data along profile A at a geoelectric strike angle of  $-57^\circ$ , using the entire period range of 0.004 – 10,000 s of both the TM- and TE-modes. The error floor was set to 30% for the apparent resistivity to account for static shift effects, and set to 7% for the phase. For each model, the smoothness parameter ( $\tau$ ) was changed after 100 iterations in order to determine the most appropriate  $\tau$  value for the dataset. The trade-off between the roughness of the model, defined by the  $\tau$  parameter, and the fit of the model to the data (Figure 17) highlights a  $\tau$  value of 7 as that which results in the smoothest model with the best fit to the data.

With an appropriate  $\tau$  value of 7, several more models were generated along profile A at a strike angle of  $-57^\circ$  using similar error floors for phase and apparent resistivity, while varying data components and parameters. Inversions of the TM-mode data alone typically result in models that identify lateral boundaries, but can be insensitive to other electrical structures that the TE-mode data better resolve. The TE-mode data are more sensitive to the conductance of structures, and better identify the depth to conductive zones or thin near-vertical low-resistivity units. Inversions were initiated with a homogeneous half space of 500 ohm-m, a mesh consisting of 64 rows and 178 columns,

and a smoothing parameter ( $\tau$ ) of 7. The parameters that were varied include using combinations of the TM and TE mode data, the smoothing parameters  $\alpha$  and  $\beta$  that trade-off vertical against horizontal gradient weighting, and the weighting of the regularization order (Figure 18 a-f). Although there are slight variations in the resistivity value and the structures, the general features are consistent between the different models. The model using both TM and TE mode data with an  $\alpha$  value of 1.0 and  $\beta$  of 1.5 (Fig. 18d) resulted in the smoothest model with the lowest RMS value, a model thus chosen for further analysis.

Overall, the RMS values, particularly when using both the TM and TE-mode data, are high. Although out-of-quadrant phases were excluded in the generation of these models, single site data with high RMS values (determined during the decomposition analysis) were not removed. The misfit value for each site for the 2-D model along profile A suggests that certain sites with anomalously high RMS values, like those at the southwest part of the profile, may be strongly influencing the overall model RMS value (Figure 19). The most problematic sites are those that resulted in high RMS values in the decomposition analysis described above. Similar models need to be generated without these data in order to assess changes in the subsurface structure and the associated RMS value. Additionally, focused models of particular areas of interest may help to further resolve structure and improve the RMS misfit. When inverting fewer data the responses to local-scale structures have a higher influence on the average misfit value and so can be better represented in the models.

One method of testing the sensitivity of the data to structure at depth is to alter the final 2-D model, run a forward inversion, and compare the resulting model RMS values. This has been done at the southwestern end of profile A to investigate the robustness of the complex multi-layer structure apparent in these preliminary 2-D models by inserting into the model a resistive block at depths between 23 and 50 km (Figure 20). In this scenario, the RMS value remained constant at 3.1 after the forward inversion, indicating that these data are not sensitive to variation within this region of the subsurface and that the apparent conductivity contrasts may be real.

## **Preliminary Interpretation and Discussion**

Although these models represent rough preliminary conductivity images, some features appear to be consistent in the data (Figures 18 and 21). The models beneath eastern Southampton Island, which exposes Precambrian rock, highlight a resistive crust to depths of  $\sim 30$  km which, in turn, is underlain by a less resistive lower crust. This contrasts with results along a profile through Melville

Peninsula for which high resistivities to depths of 35 – 39 km are derived (Spratt et al., in prep.). An apparent increase in the thickness of resistive Precambrian crust from 30 km below Southampton Island to ~40 km below Melville Peninsula to the north (*see* Figure 1), suggests a northward deepening of Rae crust across this region, consistent with recent tectonic models proposed for this region (Berman et al., 2012; Synder et al., 2012). The Southampton models show a change from laterally continuous layers below the exposed Precambrian to more complex crustal structure beneath the Paleozoic cover at the southwestern end of profile A and along the entire length of profile B. Here, resistive crust only extends to a depth of ~10 km (Fig. 18d, Fig. 20), below which an apparent a northeast-dipping conductive layer (from 5 km depth below SIG101 to 20 km depth below SIG108) is highlighted by this preliminary dataset. In this area, resistive crust correlates at surface with an outlier of mafic granulite (Figure 4). Similar lithological units, complex electrical structure and northwest-striking magnetic and gravity anomalies through this region collectively suggest that the Snowbird tectonic zone, along which deep crustal, high-P mafic granulites are exposed (Sanborn-Barrie et al. 2001; Flowers et al 2006), is contiguous across southwest Southampton Island, and keeps open the possibility of a terrane boundary in this region. Focused inversions of this region may help to further resolve these intriguing subsurface features.

The deep structure along profile A (Figure 22) shows a moderately resistive upper mantle (200-300 ohm•m) and a decrease in resistivity at depths ranging between 150 and 250 km. Given that 150-250 km approaches the maximum penetration depth estimates for this data, sensitivity testing will be important to verify the presence of features at these depths along profile A.

## Conclusions

Careful processing and analysis of MT data acquired from Southampton Island provide a good understanding of dimensionality and distortion, and show that the quality of the data is sufficient to model crustal conductivity, and in some cases lithospheric structure, beneath the survey area. Decomposition analysis shows that a geoelectric strike angle of  $-57^\circ$  is appropriate for most of the data at most of the period range along profile A and profile B, and that a strike of  $45^\circ$  and/or  $-45^\circ$  should be considered for the remaining broadband and long period data. Systematic modeling of the data using different variables has helped to determine some of the inversion parameters that should be used to provide an accurate image of the subsurface. Preliminary 1-D and 2-D models highlight:

- 1) laterally uniform, resistive crust underlies the eastern half of the island, where Precambrian rocks are exposed, to a depth of 30 km;

- 2) the resistive Precambrian crustal block appears to deepen northward, from 30 km depth below Southampton Island to ~40km depth below Melville Peninsula;
- 3) conductive upper mantle may be imaged between 150-250 km;
- 4) structurally complex upper crust below Paleozoic cover in the southwest part of the island corresponds, in part, to a resistive outlier of mafic granulite underlain by a northeast-dipping conductor and may correspond to a terrane boundary.

These models also illustrate the need for additional 2-D and 3-D inversions to further resolve the subsurface conductivity structure.

## References

- Berman R.G., Sanborn-Barrie, M, Rayner, N. and Whalen, J., 2012. The tectonometamorphic evolution of Southampton Island, Nunavut: insight from petrologic modeling and in situ SHRIMP geochronology of multiple episodes of monazite growth; *Precambrian Research*, in press
- Coyle, M., 2008. Residual total magnetic field, Southampton Island magnetic survey, Nunavut; Geological Survey of Canada, Open File 5749-5764, doi:10.4095/225211-225225
- Flowers, R.M., Bowring, S.A. and Williams, M.L., 2006. Timescales and significance of high-pressure, high-temperature metamorphism and mafic dike anatexis, Snowbird tectonic zone, Canada *Contrib. Miner. Petrol* 151 558-581.
- Groom, R.W., and R.C. Bailey, 1989: Decomposition of magnetotelluric impedance tensors in the presence of local three-dimensional galvanic distortion; *Journal of Geophysical Research*, v. 94, p. 1913 – 1935.
- Heywood, W.W. and Sanford, B.V., 1976: Geology of Southampton, Coats and Mansel Islands, District of Keewatin, Northwest Territories; Geological Survey of Canada, Memoir 382, 35p.
- Jones, A.G., 1981. Geomagnetic Induction Studies in Scandinavia - II. Geomagnetic Depth Sounding, Induction Vectors and Coast-Effect; *Journal of Geophysics*, v.50, p. 23 – 36.
- Jones, A.G., and H. Jodicke, 1984: Magnetotelluric transfer function estimation improvement by a coherence-based rejection technique, paper presented at the 54<sup>th</sup> Society of Exploration Geophysics Annual General Meeting, Atlanta, Georgia, 2-6 December, Abstract volume, pp. 51-55.
- Jones, A.G., A.D. Chave, G.D. Egbert, D. Auld, and K. Barh, 1989: A comparison of techniques for magnetotelluric response function estimation; *Journal of Geophysical Research*, v. 94, p. 14210

– 14213.

- Mackie, R.L., and T.R. Madden, 1993: Three-dimensional magnetotelluric inversion using conjugate gradients; *Geophysical Journal International*, V. 115, p. 215 – 229.
- McNeice, G.W., and A.G. Jones, 2001: Multisite, multifrequency tensor decomposition of magnetotelluric data; *Geophysics*, v. 66, p. 158 – 173.
- Menvielle, M.J.C., P. Rossignal, and P. Tarits, 1982: The coast effect in terms of deviated electric currents: A numerical study; *Physics of the Earth and Planetary Interiors*, v. 28, p. 118 – 128.
- Pous, J., Heise, W., Schegg, P.A., Munoz, G., Mart, J. and Soriano, C., 2002. Magnetotelluric study of the Las Canadas caldera (Tenerife, Canary Islands): structural and hydrogeological implications; *Earth and Planetary Science Letters*, v. 204, p. 249 – 263.
- Sanborn-Barrie, M., Carr, S.D. and Thériault, R., 2001. Geochronological constraints on metamorphism, magmatism and exhumation of deep-crustal rocks of the Kramanitar Complex, with implications for the Paleoproterozoic evolution of the Archean western Churchill Province, Canada. *Contributions to Mineralogy and Petrology* 141:592-612.
- Santos, F.A.M., Nolasco, M., Almeida, E.P., Pous, J., and Mendes-Victor, L.A., 2001. Coast effects on magnetic and magnetotelluric transfer functions and their correction: application to MT soundings carried out in SW Iberia; *Earth and Planetary Science Letters*, v.186, p. 283-295.
- Schmucker, U., 1970. Anomalies of geomagnetic variations in the southwestern United States, *Bull. Scripps Ints. Oceanogr.* v. 13, 165 p.
- Snyder, D.B., Berman, R.G., Kendall, G. and Sanborn-Barrie, M., 2012. Seismic anisotropy and mantle structure of the Rae craton, central Canada, from joint interpretation of SKS splitting and receiver functions. *Precambrian Research*,
- Spratt, J.E., Jones, A.G., Corrigan, D., Hogg, D., 2012 Lithospheric geometry beneath Melville Peninsula, Nunavut, revealed. *Current Research, in prep.*
- Zhang, S. 2008. New insights into the Ordovician oil shales in Hudson Bay Basin: their number, stratigraphic position, and petroleum potential; *Bulletin of Canadian Petroleum Geology*, v. 56, n. 4, p. 300 - 324.

## Figure Captions

Figure 1: Regional map illustrating the locations of MT surveys in eastern Nunavut: CBEX= the

Central Baffin Magnetotelluric Experiment, MPMT = Melville Peninsula Magnetotelluric survey, SIIGMT = Southampton Island Integrated Geoscience Magnetotelluric survey, DMT1 = Diamonds Magnetotelluric survey: corridor 1, CPMT - Cumberland Peninsula Magnetotelluric survey, and STZMT - Snowbird Tectonic Zone Magnetotelluric survey.

Figure 2: Simplified geological map of Southampton Island showing the location of magnetotelluric sites recorded. Circles mark the locations of the response curve examples shown in figure 4. The grey lines show the position of the profiles used for 2D modelling.

Figure 3: Examples of apparent resistivity and phase MT response curves for data measured at 4 sites: (a) broadband data from site SIG109 on profile A; (b) long period data from site SIG202, northeast end of profile A; (c) merged broadband and long period data from site SIG202, central Southampton Island, and (d) an example of data distortion at site SIG111, southwest end of profile A, causing the phases of one mode to be out of quadrant.

Figure 4: Detailed geological map of Southampton Island showing mapped structural features in relation to MT site locations. The black circles mark the sites that have out-of-quadrant phases at a strike angle of  $-57^\circ$ .

Figure 5: Examples of results of single-site, single-frequency decomposition analysis where no strike angle could be reliably determined: (a) data from site SIG008 with acceptably low RMS misfit but with strong twist and shear variations, (b) and (c) show examples of site data with high RMS values corresponding to high twist and shear values, suggestive of the presence of local 3-D distortion.

Figure 6: Maps showing the preferred geoelectric strike direction with a  $90^\circ$  ambiguity at each site for single decade period bands. The color scale illustrates the maximum difference between the TM- and TE-mode phases (phase difference). The insets in c) and e) display the rotation implied by the geoelectric strike referred to in the text for  $33^\circ$  and  $45^\circ$ , respectively.

Figure 7: Map of Southampton Island highlighting the degree of correspondence between magnetically defined near-surface structure and geoelectric strike direction. The arrows show the preferred geoelectric strike direction at the 0.01 - 0.1 s bandwidths (Fig. 7a) and the 10 - 100 s period bandwidths (Fig. 7b). For both, the length of the arrow is scaled by the maximum phase difference between the TM and TE modes.

Figure 8: Map of Southampton Island highlighting the degree of correspondence between regional gravity data and geoelectric strike direction. The arrows show the preferred geoelectric strike direction at the 0.01 - 0.1 s and 0.1 - 1 s period bandwidths, and the length of the arrow is scaled by the maximum phase difference between the TM and TE modes.

Figure 9: Data misfit values at sites along profile A over the whole recorded period range for data recalculated at a geoelectric strike direction of 16° (a), 33° (b), and 45° (c). The red ellipses mark areas that do not fit at any strike angle, evidence for distortion. The black ellipses mark sites that showed either high RMS values or highly variable twist and shear values in the single-site, single-frequency decomposition analysis.

Figure 10: Data misfit values at sites along profile B over the whole recorded period range, for data recalculated at a geoelectric strike direction of 16° (a), 33° (b), and 45° (c). The red ellipses mark the areas that do not fit at any strike angle. The black ellipse marks site SIG112, that showed high RMS values in the single-site, single-frequency decomposition analysis.

Figure 11: Data misfit values at the northernmost broadband sites and the long period sites over the whole recorded period range, for data recalculated at a geoelectric strike direction of 16° (a), 33° (b), and 45° (c). The red ellipse marks the area that does not fit at any strike angle. The black ellipses mark sites that showed highly variable twist and shear values at short periods in single-site, single-frequency decomposition analysis.

Figure 12: Estimates of maximum penetration depths for each site along profile A (a), profile B (b), and the northern broadband and long period sites (c) in both the mutually perpendicular XY and YX modes.



Grey circles mark sites where phases are out of quadrant, an indication of distortion.

Figure 13: A 3-D mesh of the MT survey area showing simplified land versus ocean conductivity contrast. Examples of the forward calculated response curves are shown for profile A (SIG101, SIG103), profile B (SIG117), remote broadband (SIG010) and remote long period (SIG204) sites.

Figure 14: Cross-sectional results of 1-D modelling for profile A. a) Occam inversion analysis (b) pseudosections of the phases with increasing period of both the TE- and TM-modes.

Figure 15: Cross-sectional results of 1-D modelling for profile B. (a) Occam inversion analysis; (b) pseudosections of the phases along profile B with increasing period of both the TE- and TM-modes.

Figure 16: Results of 1-dimensional Occam inversions of the northernmost broadband sites and the long period sites for both the TM- and TE-modes.

Figure 17: Graph illustrating the trade-off between the RMS misfit of the model to the data and the tau value of the inversion. The tau value chosen for subsequent 2-D models is 7.

Figure 18: Preliminary 2-D models of the MT data along profile A, at a strike angle of  $-57^\circ$ , using various data components and variables after 100 iterations. The TM-only data and the TM+TE data were used with an alpha value of 1 and a beta value of 1 (a), and (b). The TM-only data and the TM+TE data were used with an alpha value of 1 and a beta value of 1.5 (c) and (d). The TM-only and the TM+TE data were used with an alpha value of 1 and beta value of 0.3 (e) and (f).

Figure 19: RMS values at each site along profile A for the model shown in figure 18d. Blue squares indicate statistically acceptable values along much of profile A, red squares highlight sites that deviate from acceptable values.

Figure 20: Altered 2-D model along profile A generated to test the sensitivity of the data at depths beneath the southwestern-most sites.

Figure 21: Preliminary 2-D models of the MT data along profile B, at a strike angle of  $-57^\circ$  using various data components and variables after 100 iterations. The TM-only data and the TM+TE data were used with an alpha value of 1 and a beta value of 1 (a), and (b). The TM-only data and the TM+TE data were used with an alpha value of 1 and a beta value of 1.5 (c) and (d).

Figure 22: Preliminary 2-D model of the MT data along profile A, at a strike angle of  $-57^\circ$ , shown to 300 km depth.

Site Name	Data Range	Latitude	Longitude	Start Date	Start Time	End Date	End Time	Duration of acquisition
SIG002	BBMT	-85.007861	63.837750	17/08/2007	14:00	17/08/2007	21:36	7.6 hours
SIG003	BBMT	-84.821694	63.999944	18/08/2007	17:24	19/08/2007	15:20	21.9 hours
SIG004	BBMT	-84.703556	64.086806	18/08/2007	22:56	19/08/2007	19:08	20.2 hours
SIG005	BBMT	-84.563444	64.198639	19/08/2007	17:32	20/08/2007	13:28	19.9 hours
SIG006	BBMT	-84.438389	64.294889	19/08/2007	20:49	20/08/2007	18:22	21.5 hours
SIG007	BBMT	-84.308472	64.420139	20/08/2007	16:13	21/08/2007	14:00	21.8 hours
SIG008	BBMT	-84.461361	64.679056	20/08/2007	20:46	21/08/2007	14:01	17.3 hours
SIG009	BBMT	-84.729556	64.756222	21/08/2007	17:10	22/08/2007	14:00	20.8 hours
SIG010	BBMT	-84.981528	64.801389	21/08/2007	22:45	22/08/2007	18:00	19.2 hours
SIG011	BBMT	-84.935050	63.910300	25/08/2007	15:14	25/08/2007	18:23	3.2 hours
SIG012	BBMT	-85.054767	63.786317	25/08/2007	16:46	25/08/2007	17:57	1.2 hours
SIG013	BBMT	-84.111778	64.579722	16/08/2007	21:29	17/08/2007	13:02	15.6 hours
SIG101	BBMT	-85.106389	63.763972	12/07/2008	23:00	14/07/2008	15:24	40.4 hours
SIG102	BBMT	-85.040722	63.795861	12/07/2008	23:00	14/07/2008	16:14	41.2 hours
SIG103	BBMT	-84.327556	64.387528	14/07/2008	19:00	16/07/2008	12:18	41.3 hours
SIG104	BBMT	-84.211139	64.502944	14/07/2008	20:00	17/07/2008	11:49	63.8 hours
SIG105	BBMT	-84.666667	64.119472	19/07/2008	19:00	21/07/2008	15:50	44.8 hours
SIG106	BBMT	-84.776806	64.037611	19/07/2008	21:00	21/07/2008	16:20	43.3 hours
SIG107	BBMT	-84.844583	63.972361	21/07/2008	18:00	23/07/2008	02:00	32.0 hours
SIG108	BBMT	-84.894667	63.921222	21/07/2008	20:00	23/07/2008	16:23	44.4 hours
SIG109	BBMT	-84.966944	63.881861	23/07/2008	18:00	26/07/2008	15:11	69.2 hours
SIG110	BBMT	-85.191306	63.723472	23/07/2008	20:00	25/07/2008	17:41	45.7 hours
SIG111	BBMT	-85.235556	63.683278	26/07/2008	17:00	28/07/2008	09:37	40.6 hours
SIG112	BBMT	-84.755694	63.664361	26/07/2008	19:00	28/07/2008	03:23	32.4 hours
SIG113	BBMT	-84.599472	63.791333	29/07/2008	20:00	01/08/2008	03:04	55.1 hours
SIG114	BBMT	-84.653389	63.748750	29/07/2008	18:30	01/08/2008	08:10	61.7 hours
SIG115	BBMT	-84.697778	63.702722	29/07/2008	17:30	01/08/2008	02:01	56.5 hours
SIG116	BBMT	-84.538278	63.864972	01/08/2008	22:00	04/08/2008	06:40	56.7 hours
SIG117	BBMT	-84.464139	63.926500	01/08/2008	23:00	03/08/2008	13:02	38.0 hours
SIG201	LMT	-84.471667	65.280556	09/07/2008	01:00	17/07/2008	19:15	8.76 days
SIG202	LMT	-84.114167	64.576944	09/07/2008	01:00	23/07/2008	09:01	14.3 days
SIG203	LMT	-84.273333	64.924444	11/07/2008	01:00	25/07/2008	00:28	14.0 days
SIG204	LMT	-81.932500	64.275833	10/07/2008	01:00	16/07/2008	01:44	6.0 days
SIG205	LMT	-83.245556	64.151389	23/07/2008	20:00	28/07/2008	17:13	4.1 days
SIG206	LMT	-83.887222	64.105556	26/07/2008	20:00	01/08/2008	21:26	6.0 days

Table 1: Site type, location, and recording times for each of the MT sites on Southampton Island.

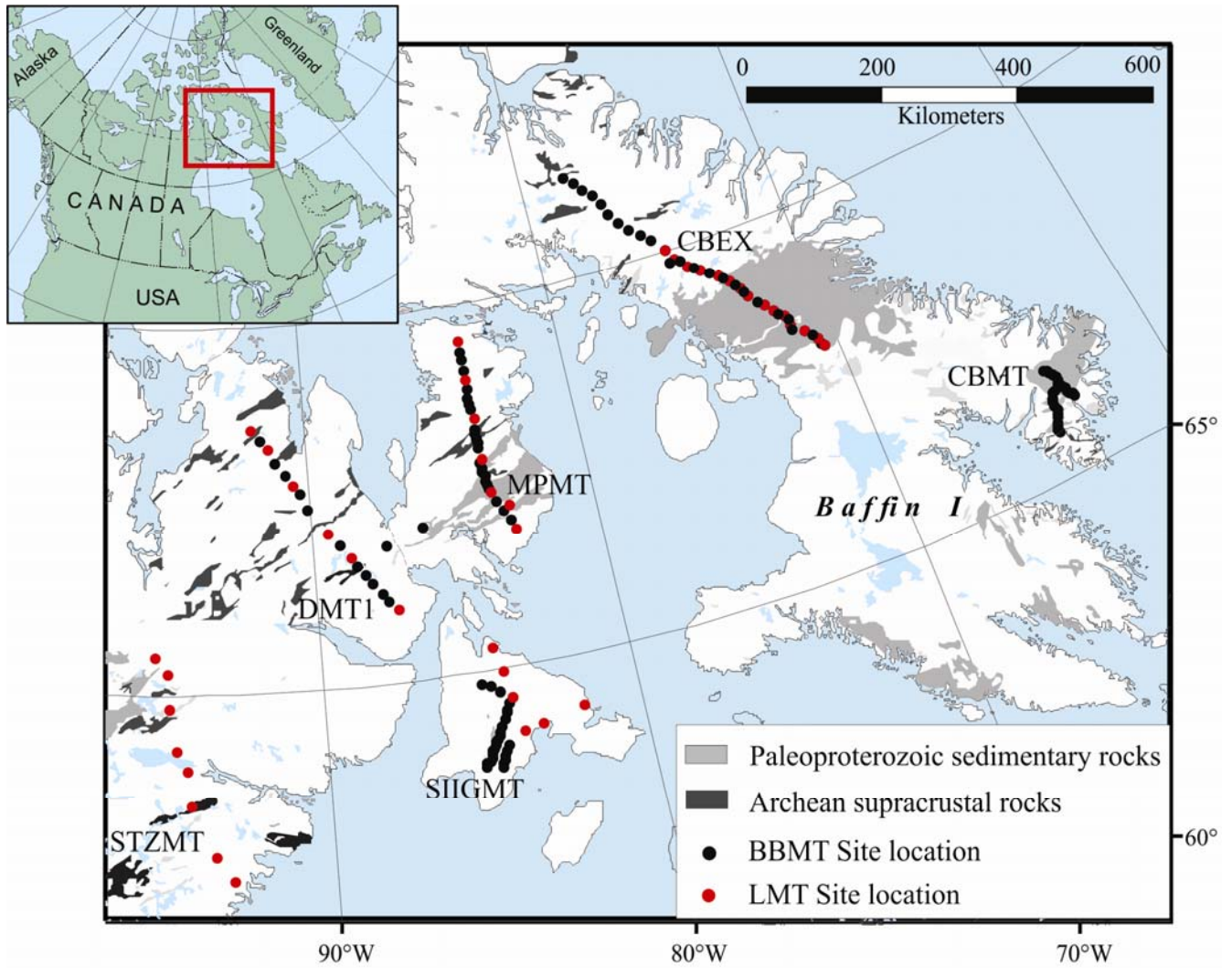


Figure 1

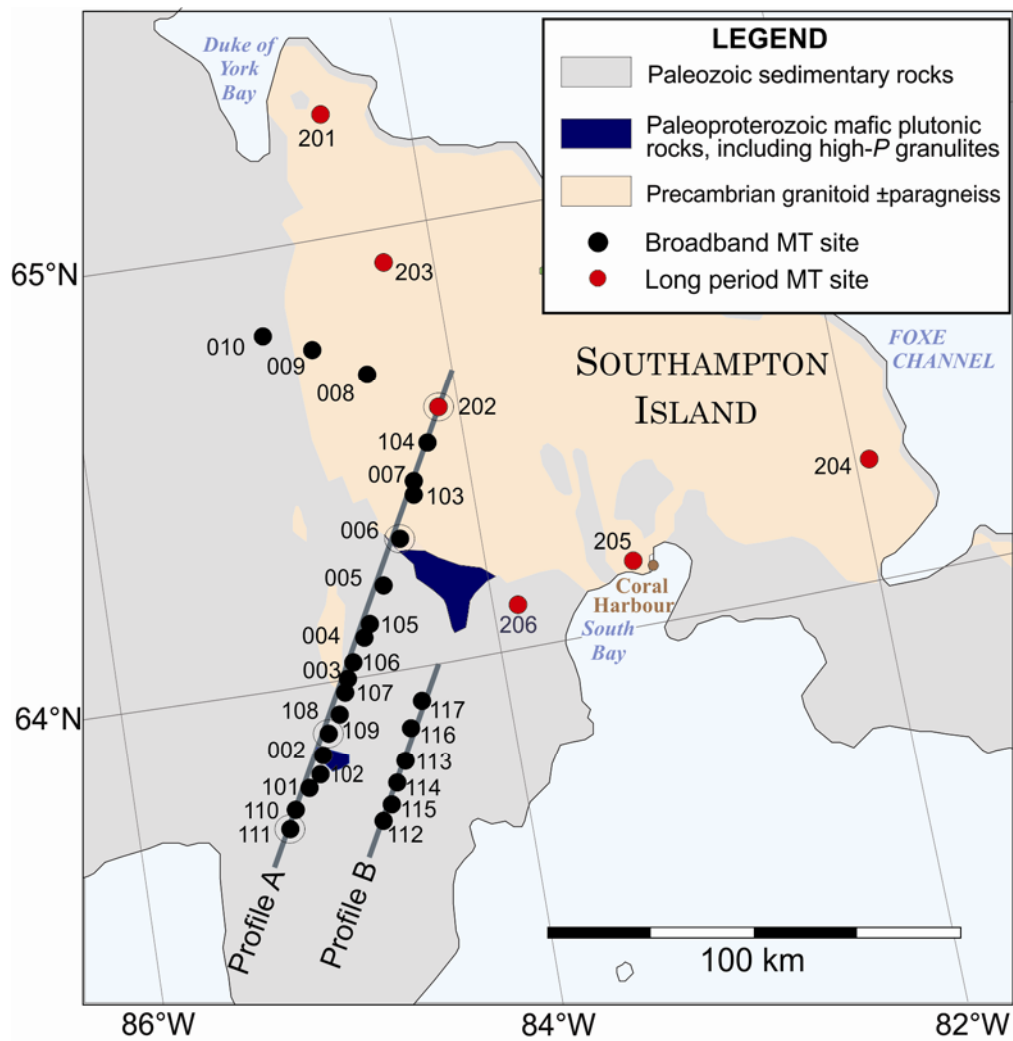


Figure 2

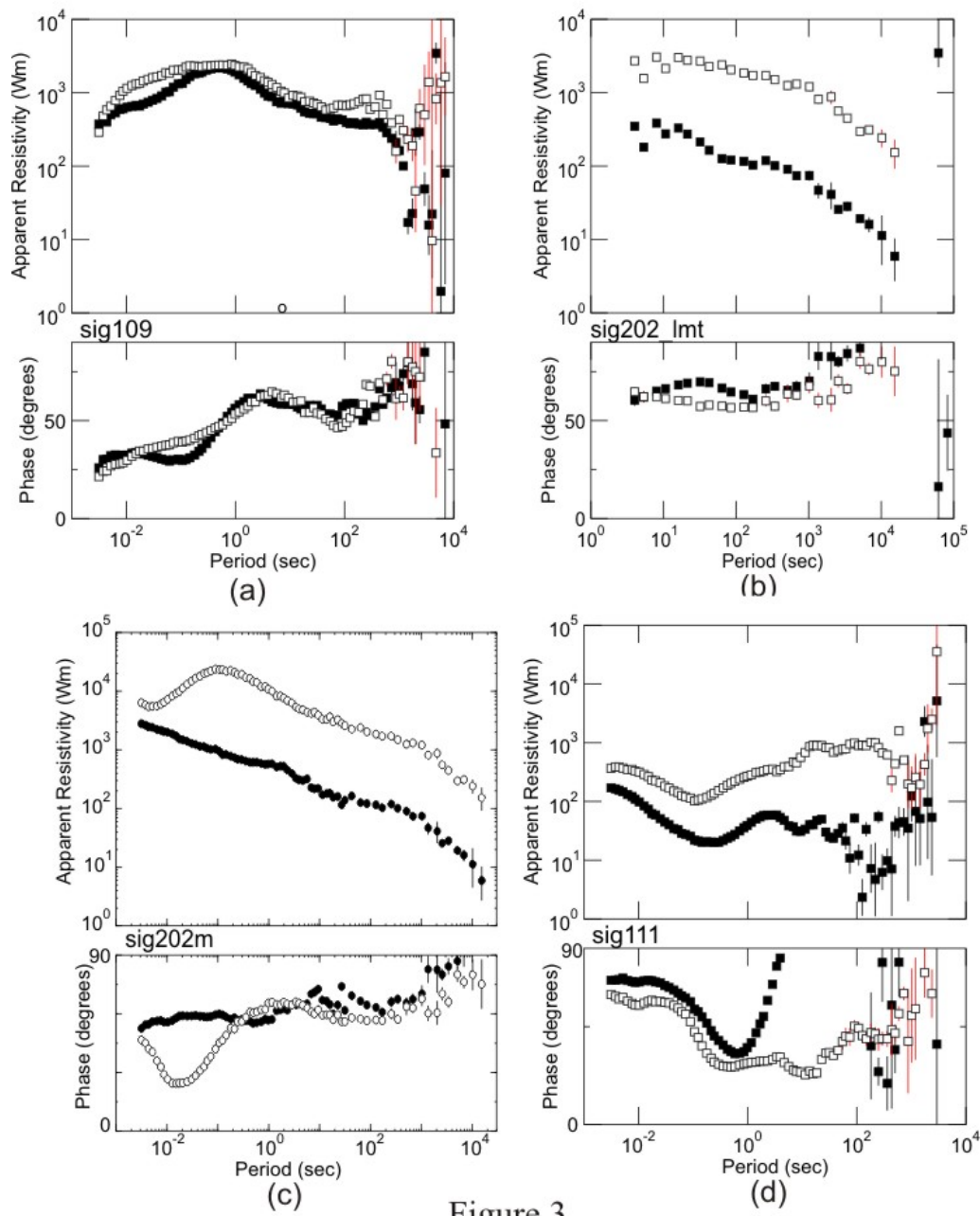


Figure 3

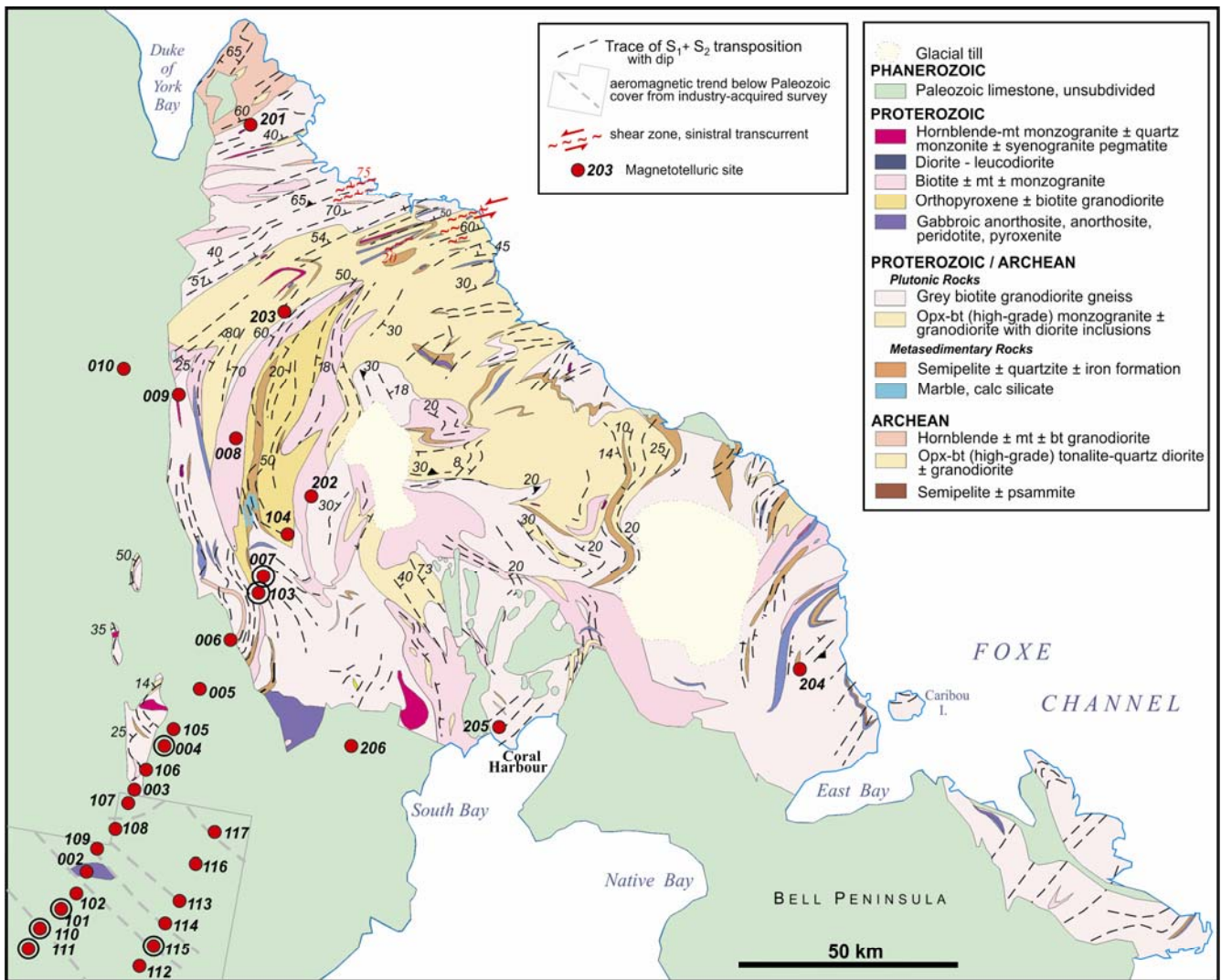


Figure 4

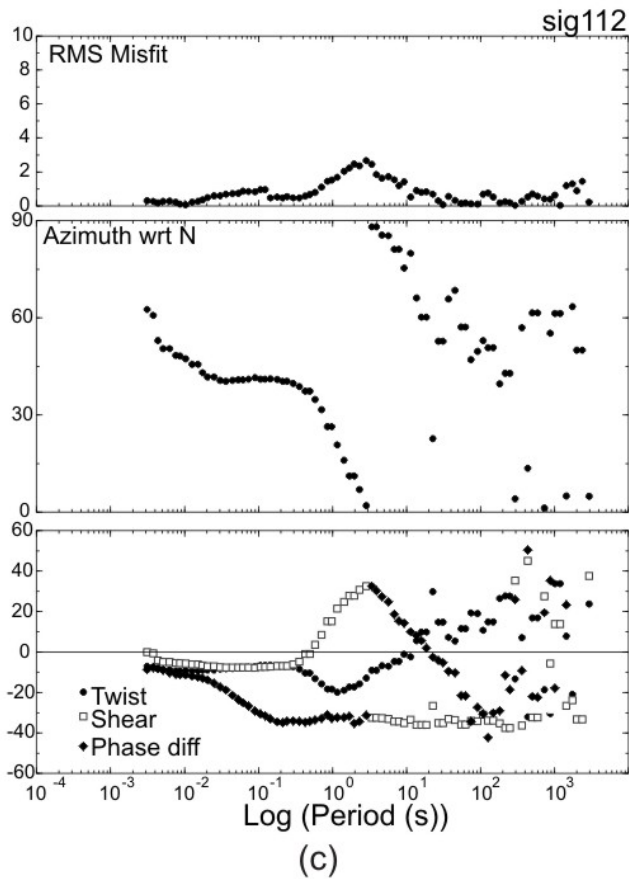
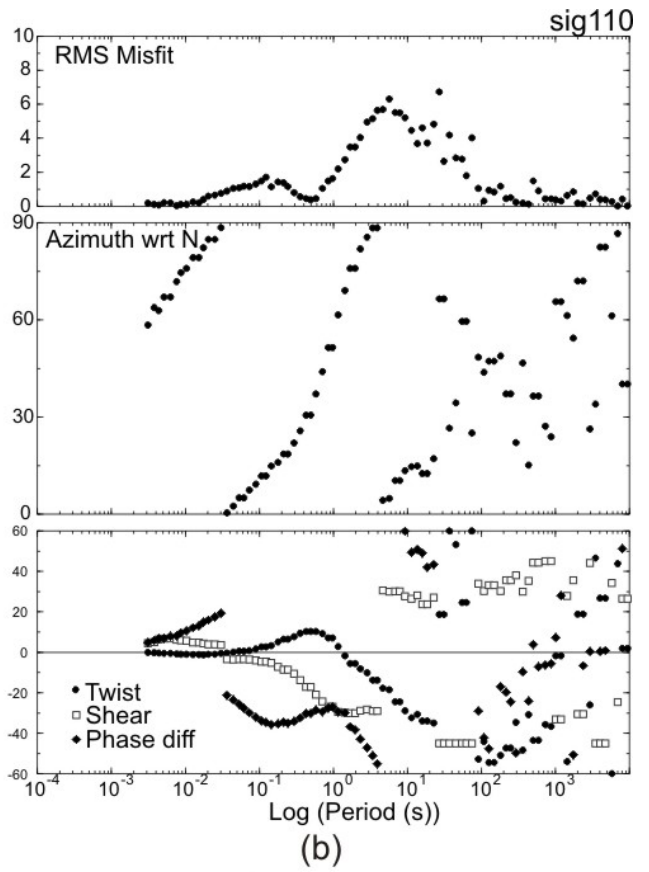
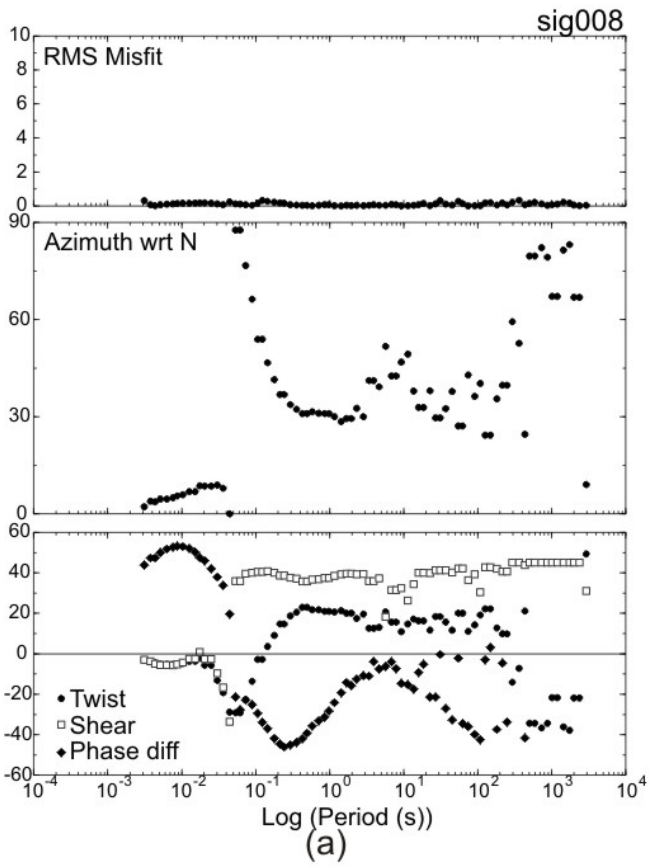


Figure 5



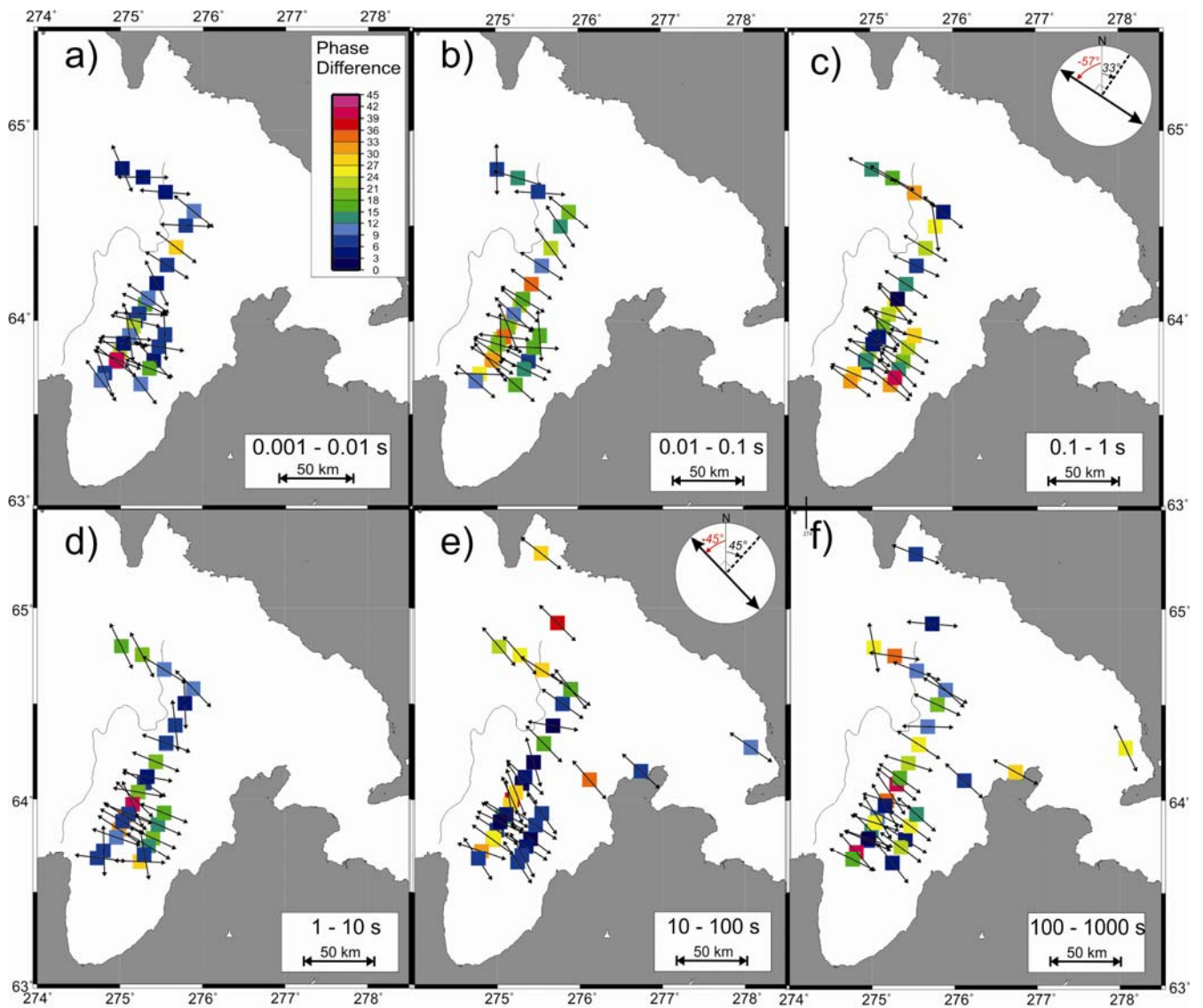


Figure 6

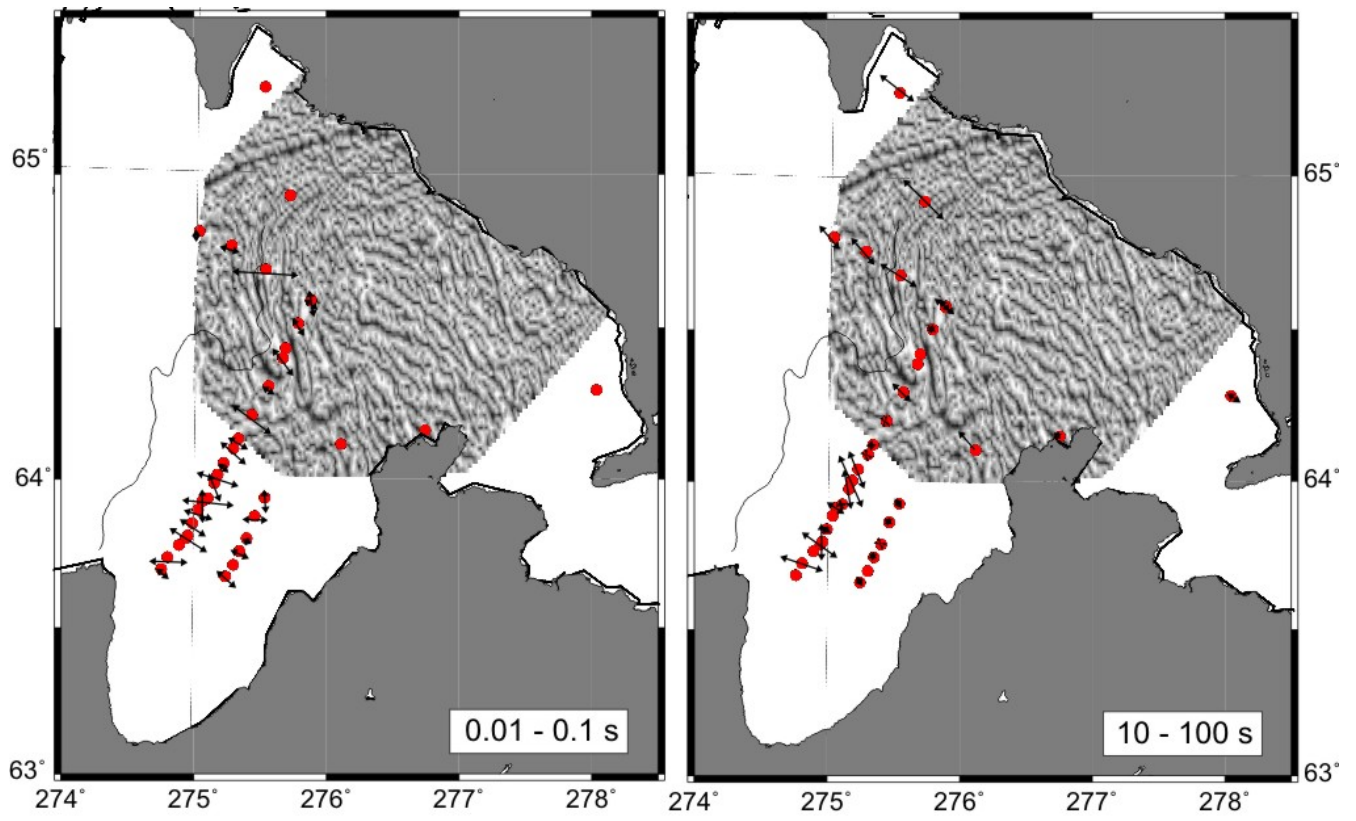


Figure 7

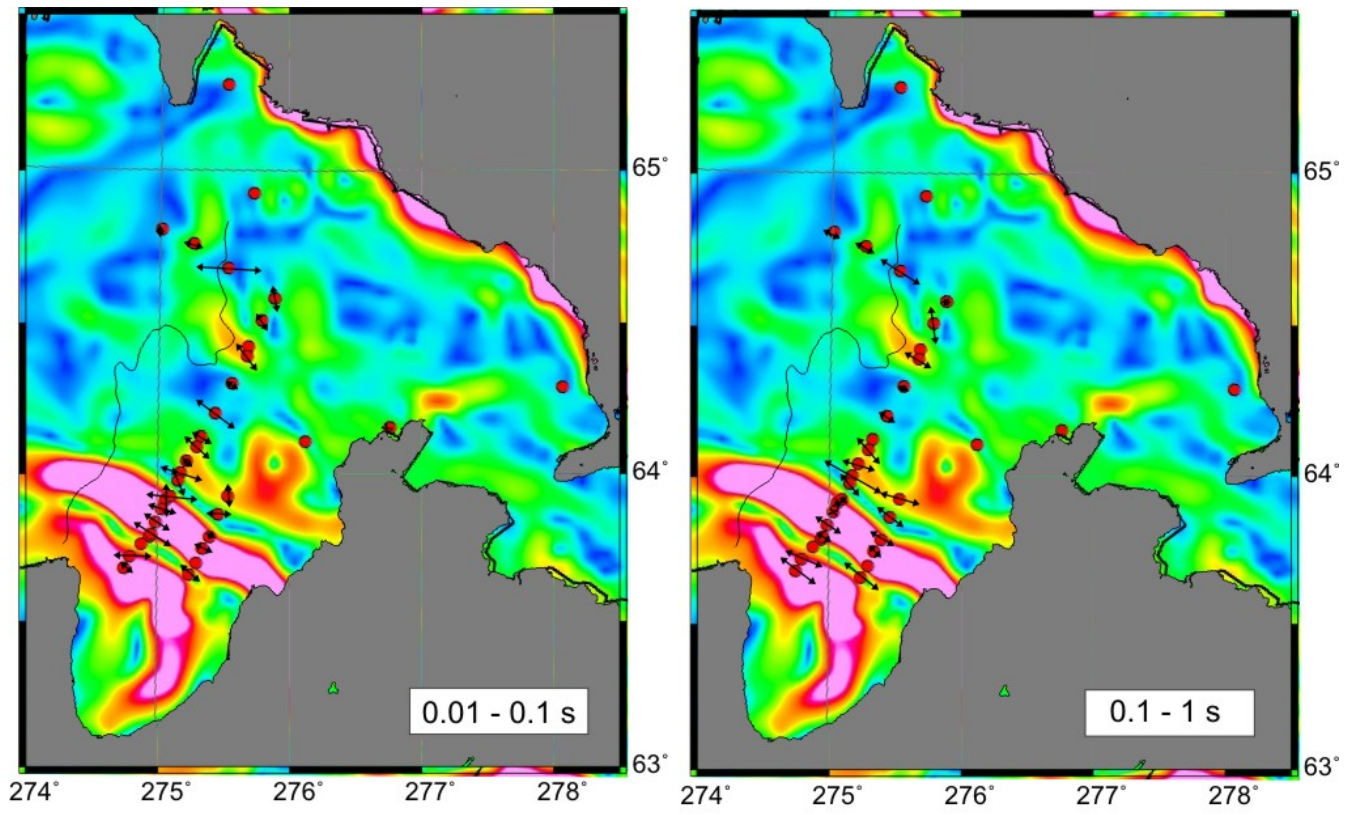


Figure 8

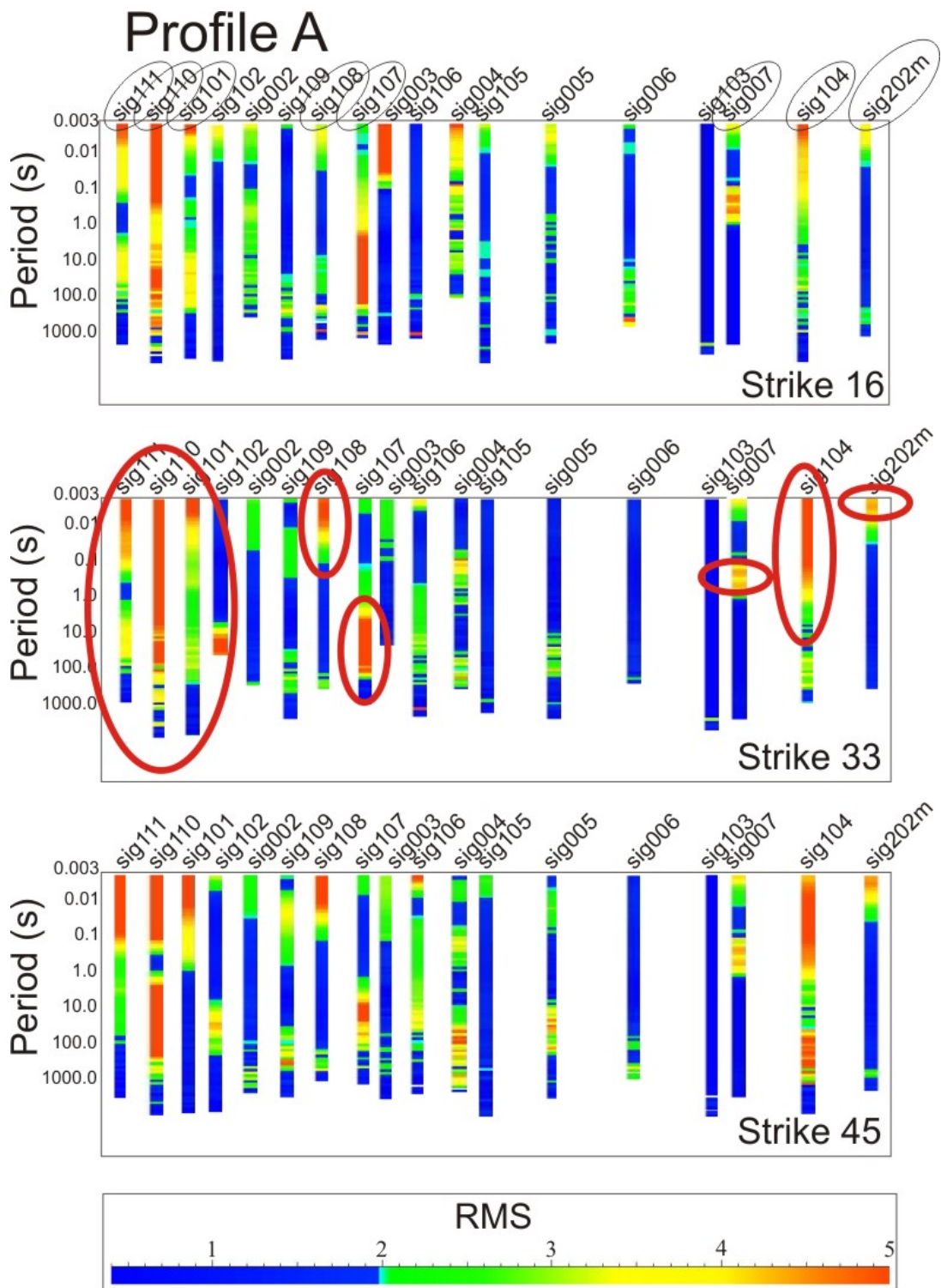


Figure 9

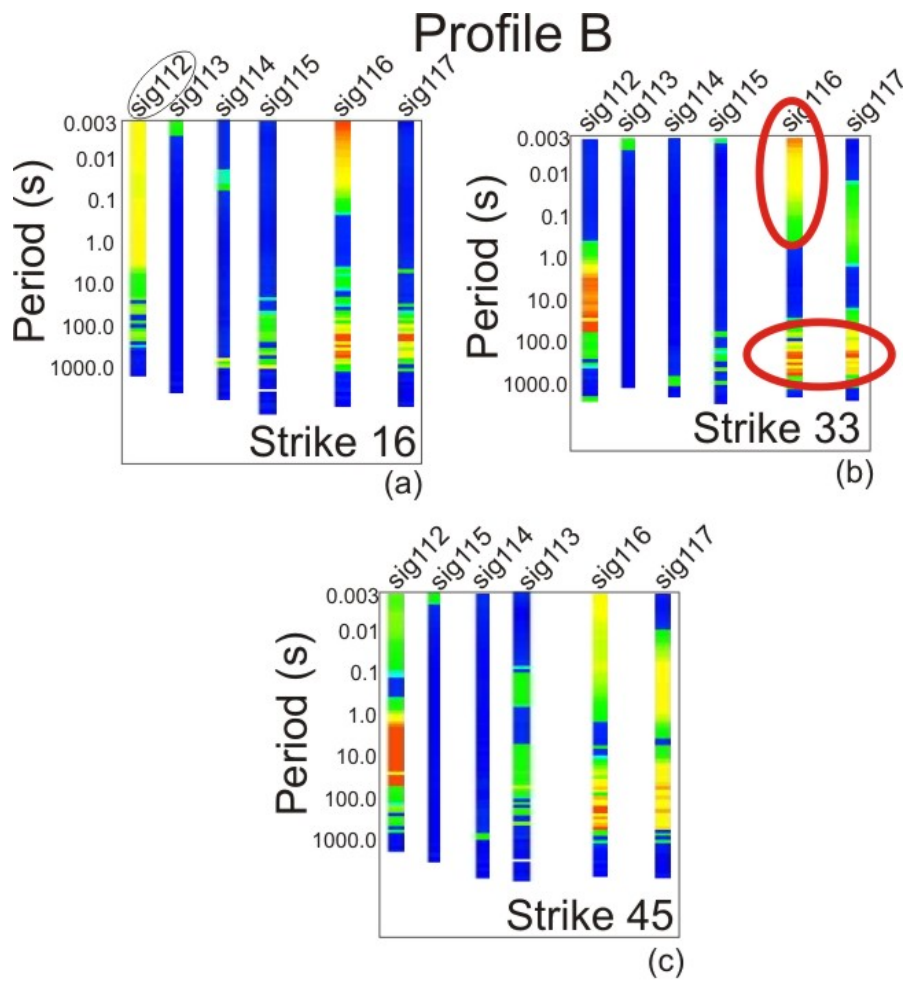


Figure 10

# Northern and Long Period Sites

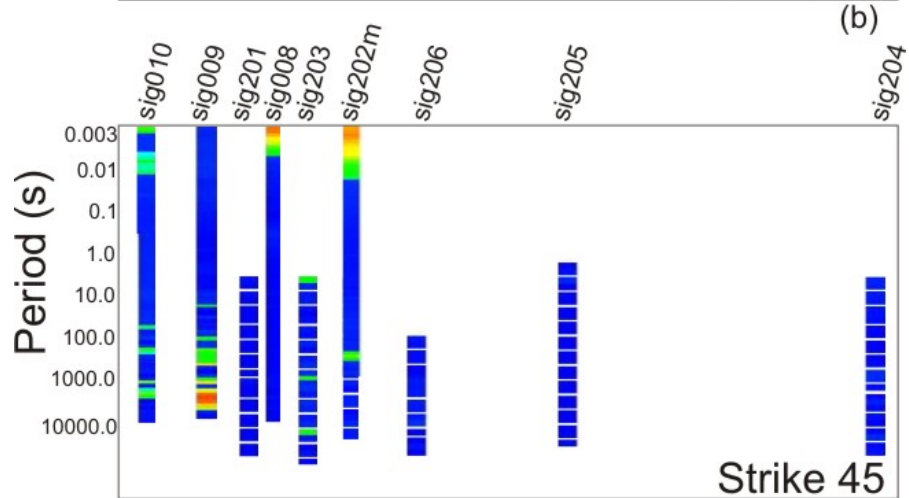
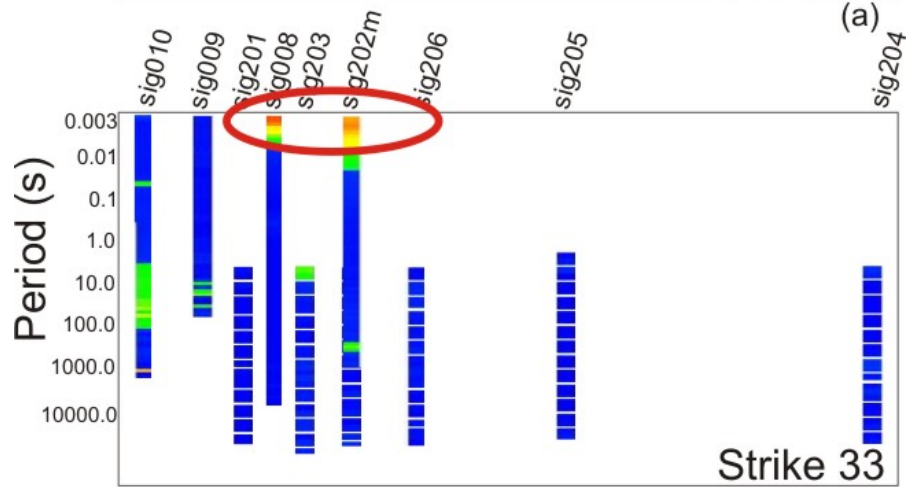
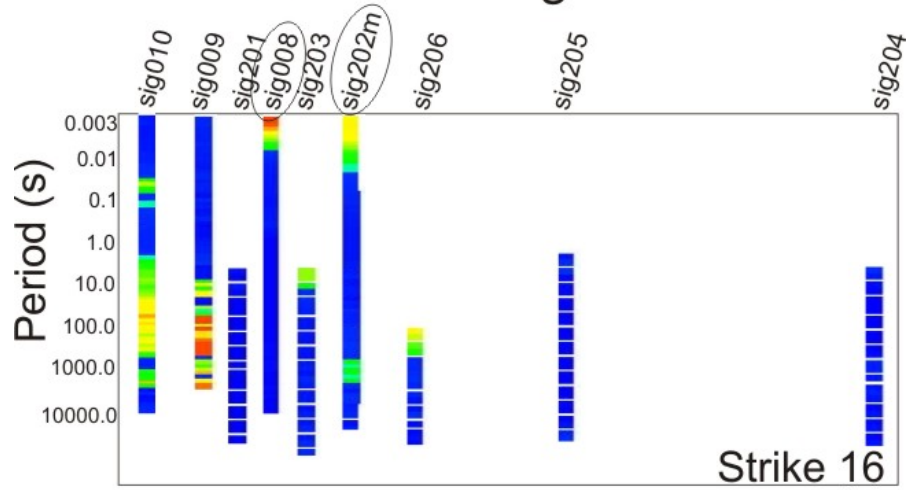


Figure 11

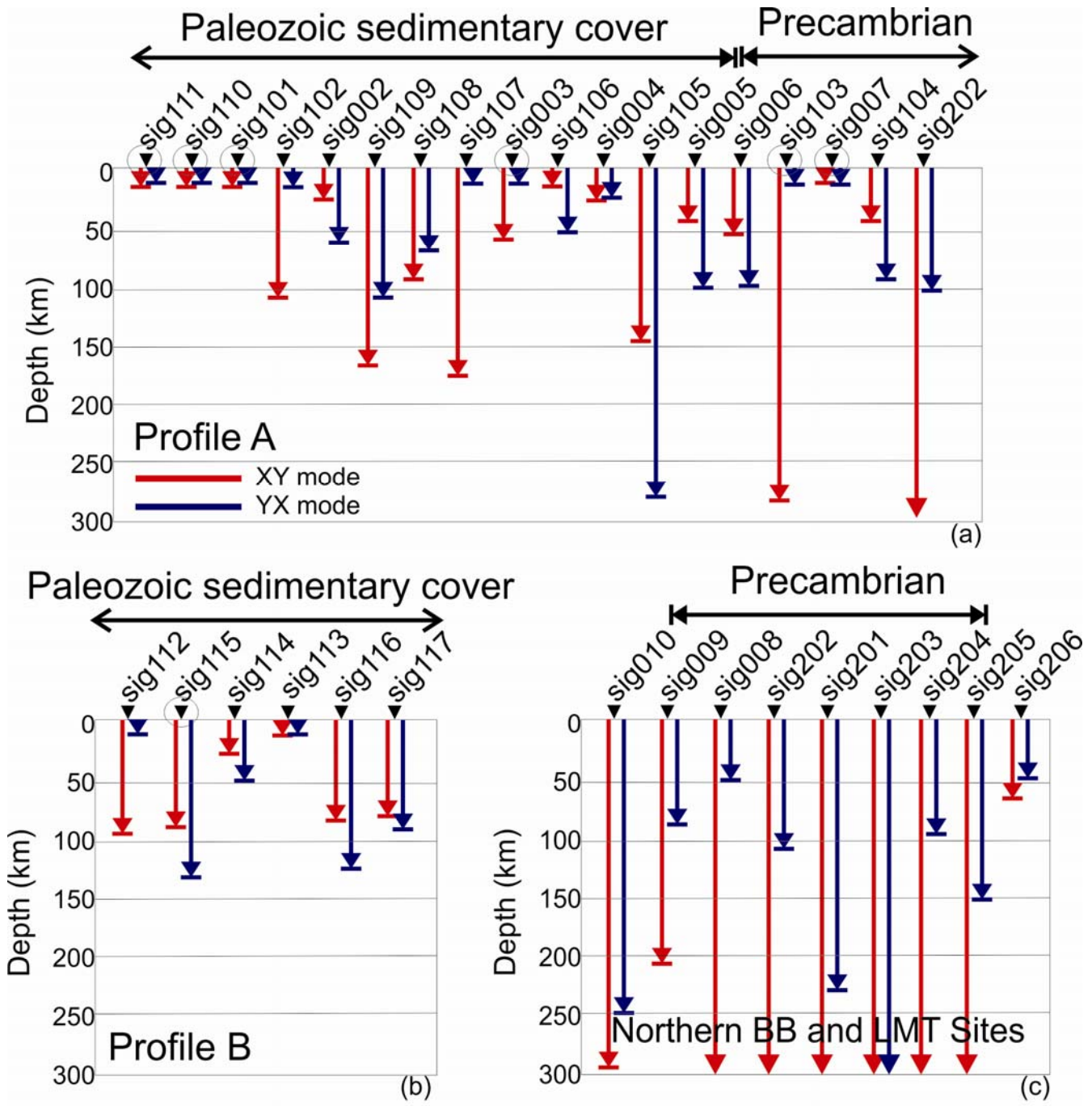


Figure 12

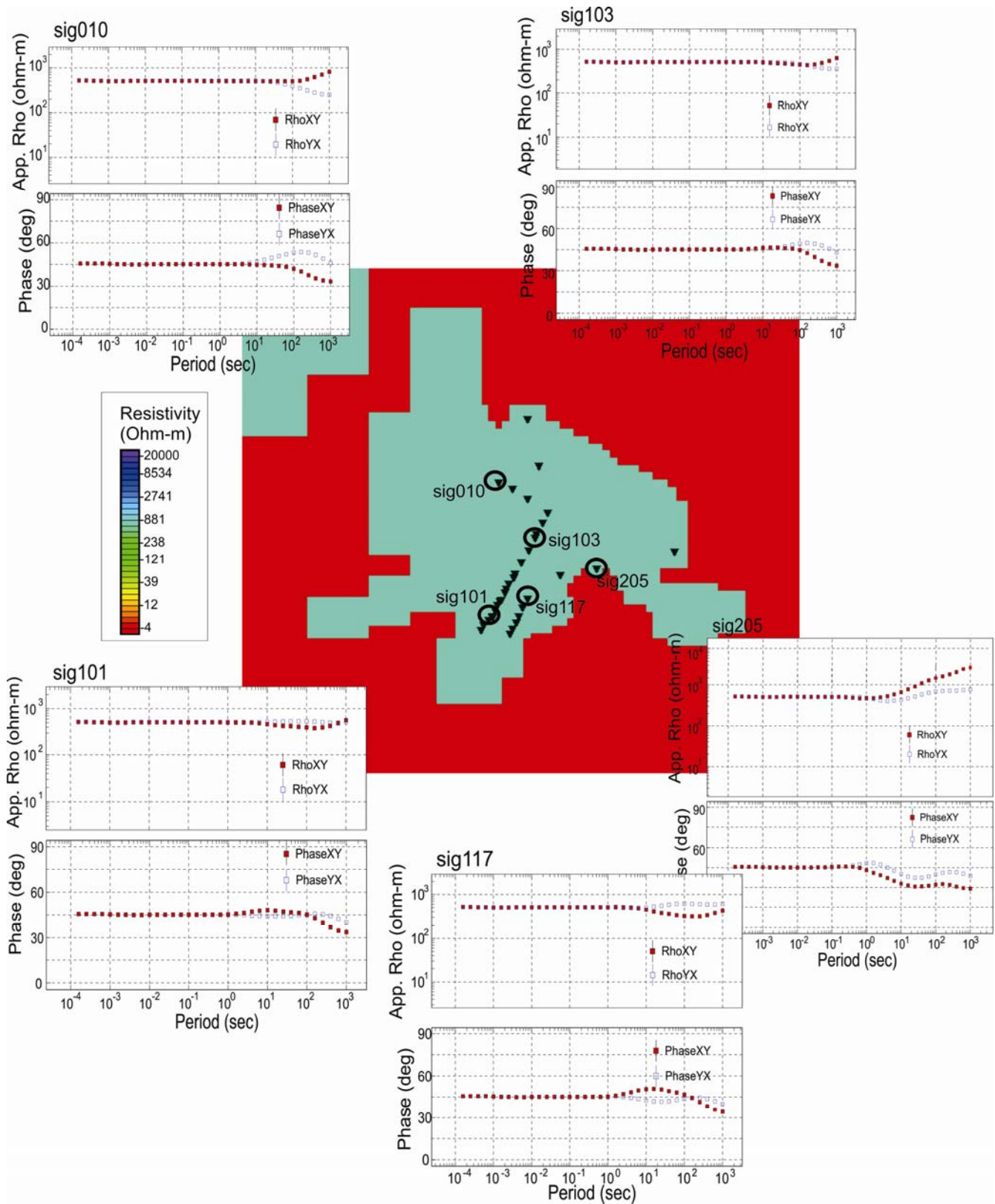


Figure 13



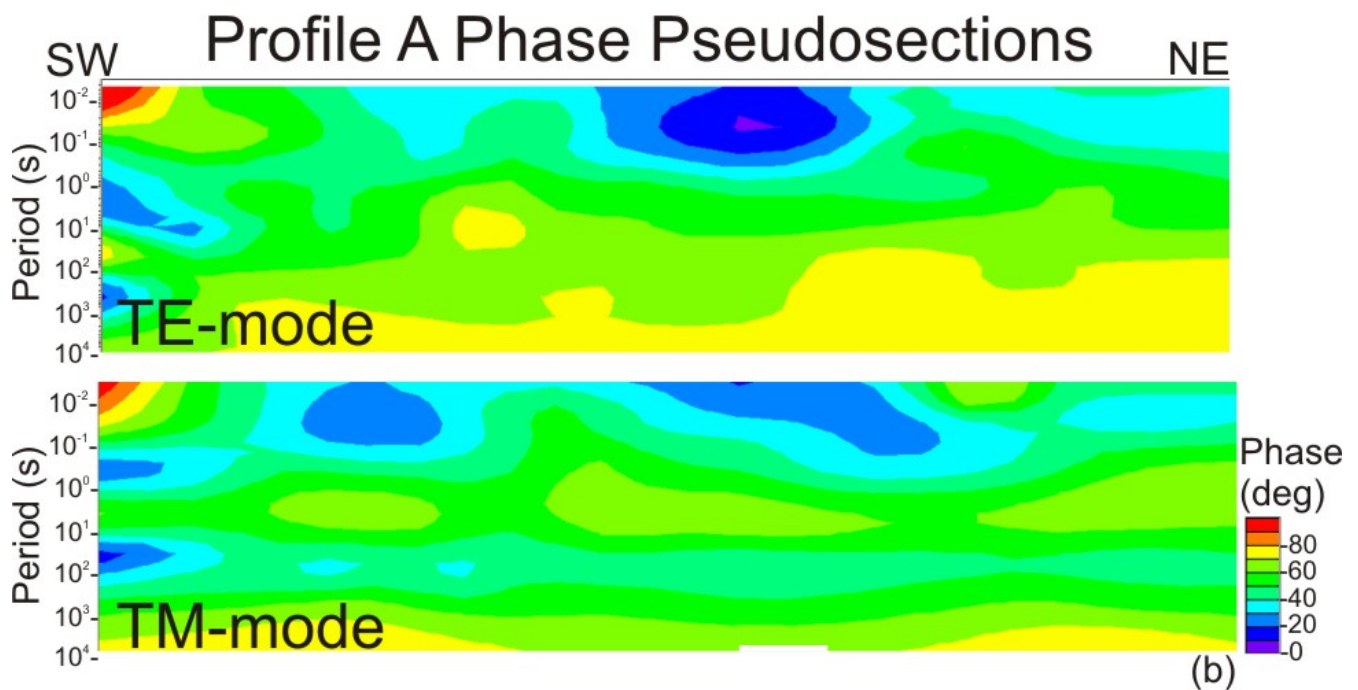
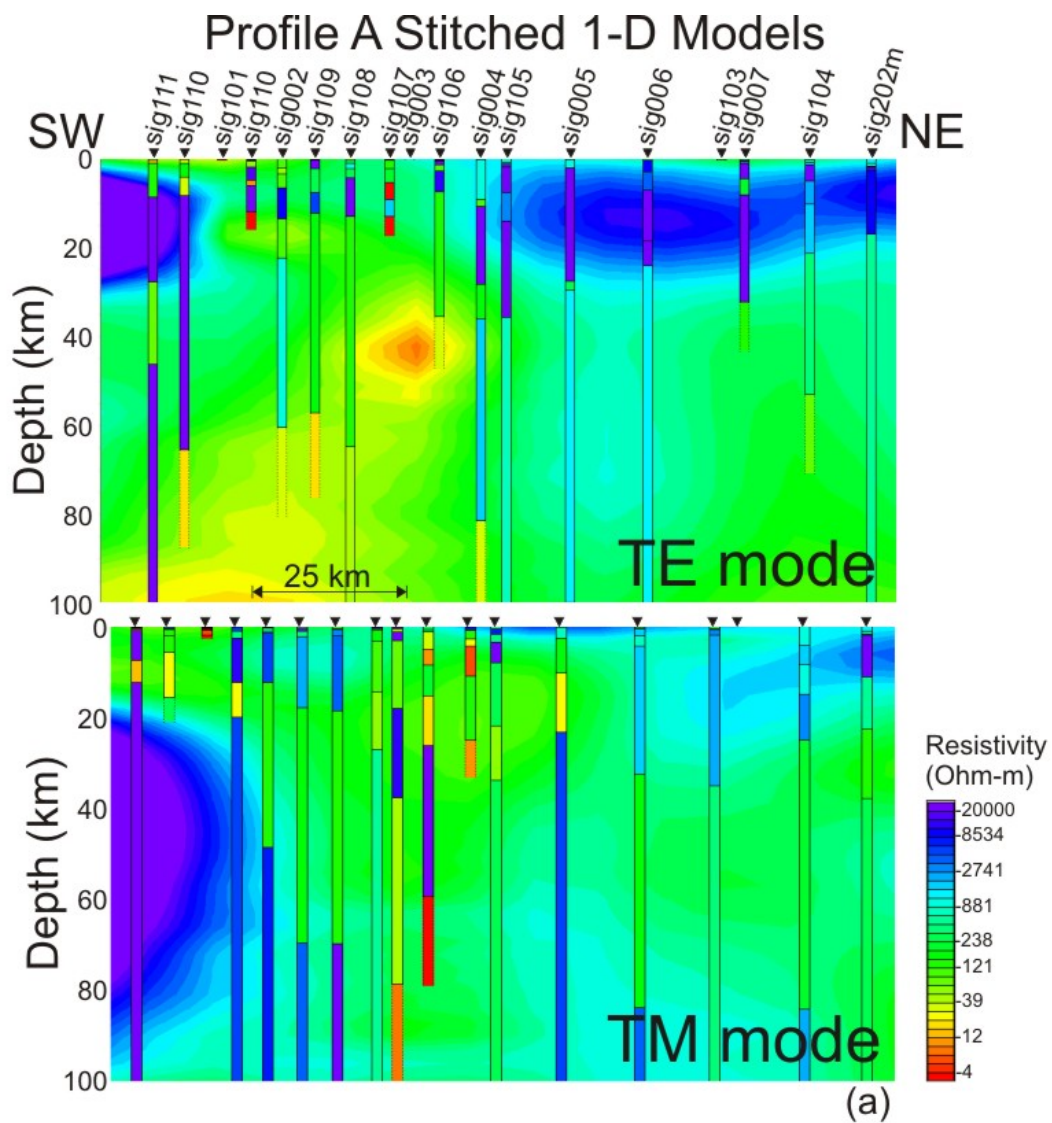


Figure 14

# Profile B Stitched 1-D Models

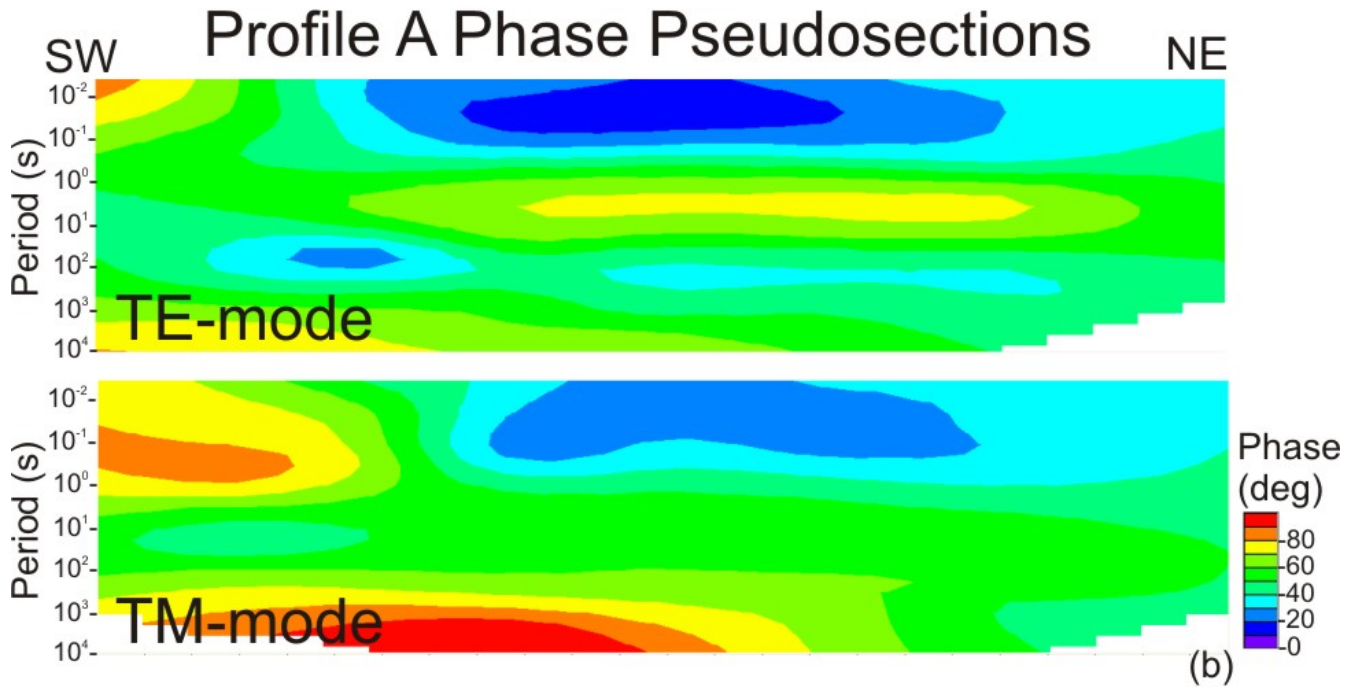
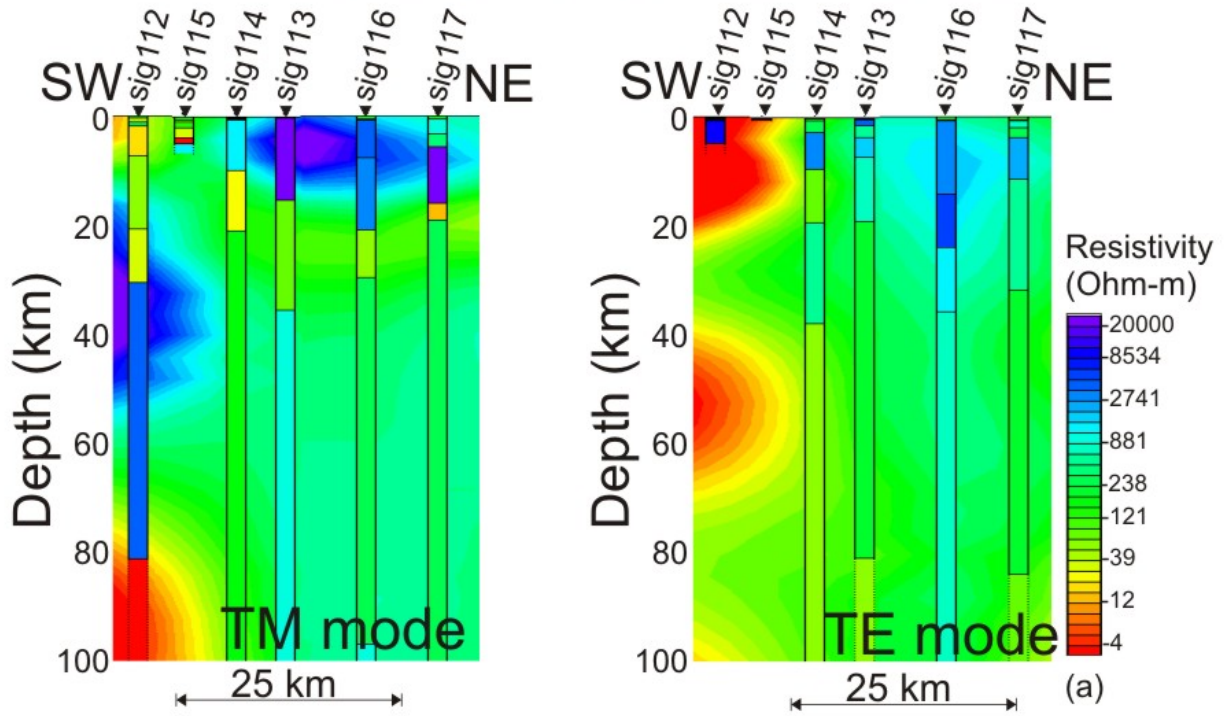


Figure 15

# 1-D Models for Northern Broadband and Long Period Sites

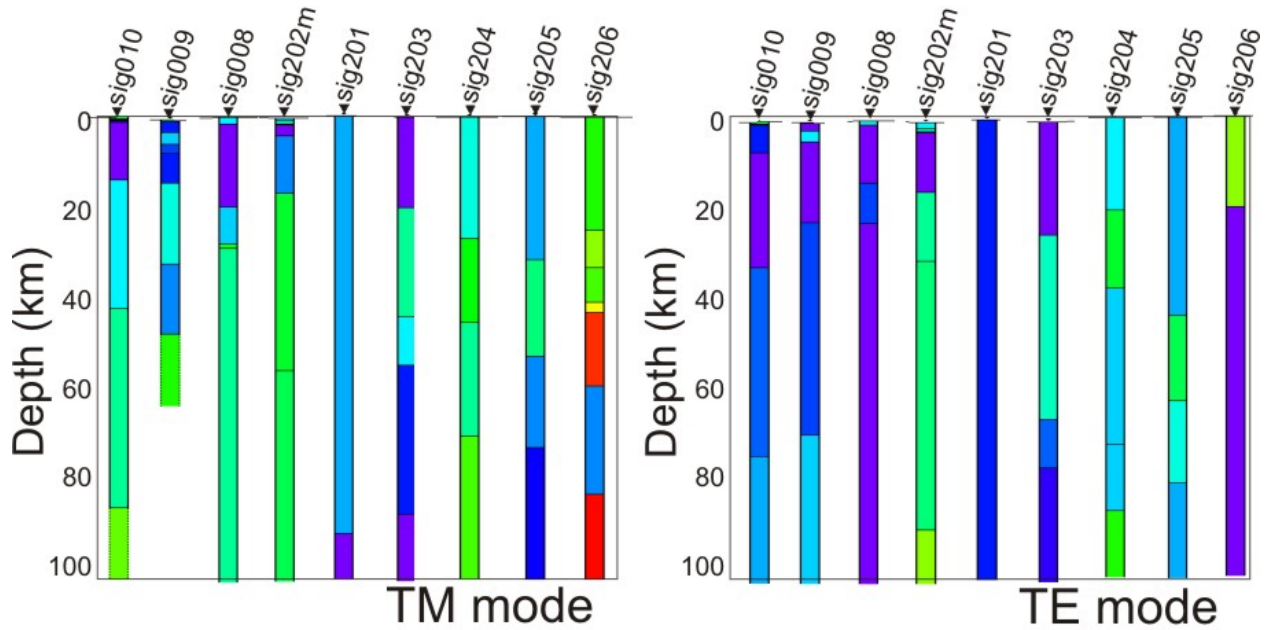


Figure 16

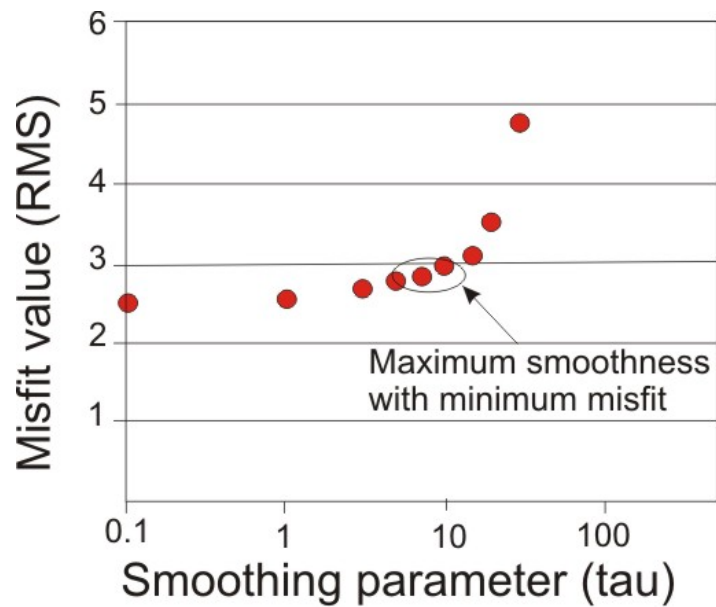


Figure 17

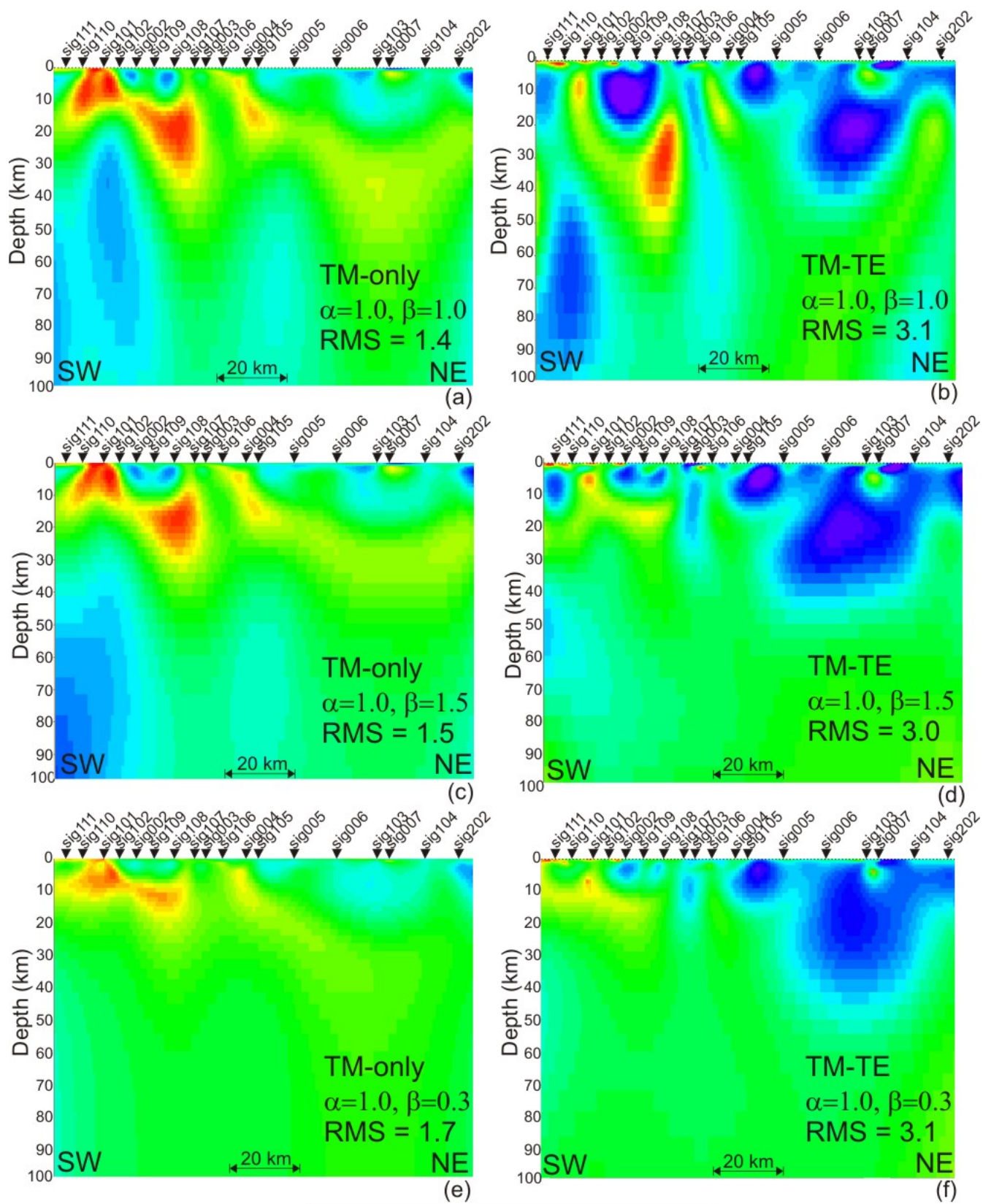


Figure 18

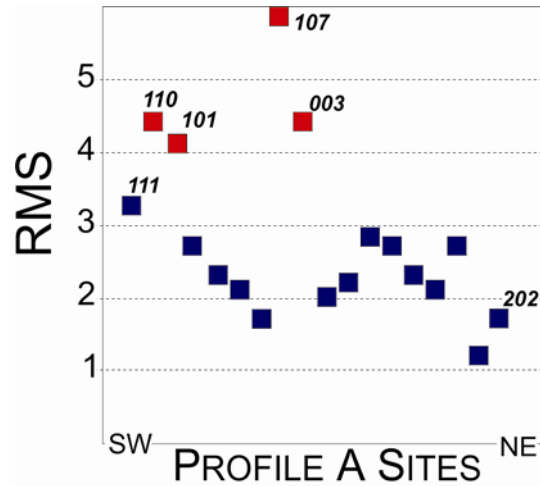


Figure 19

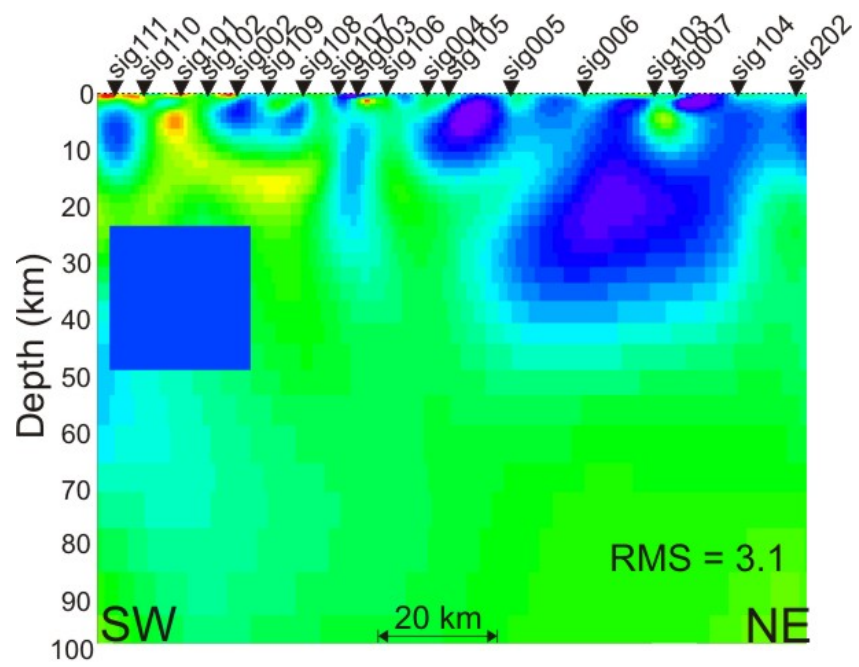


Figure 20

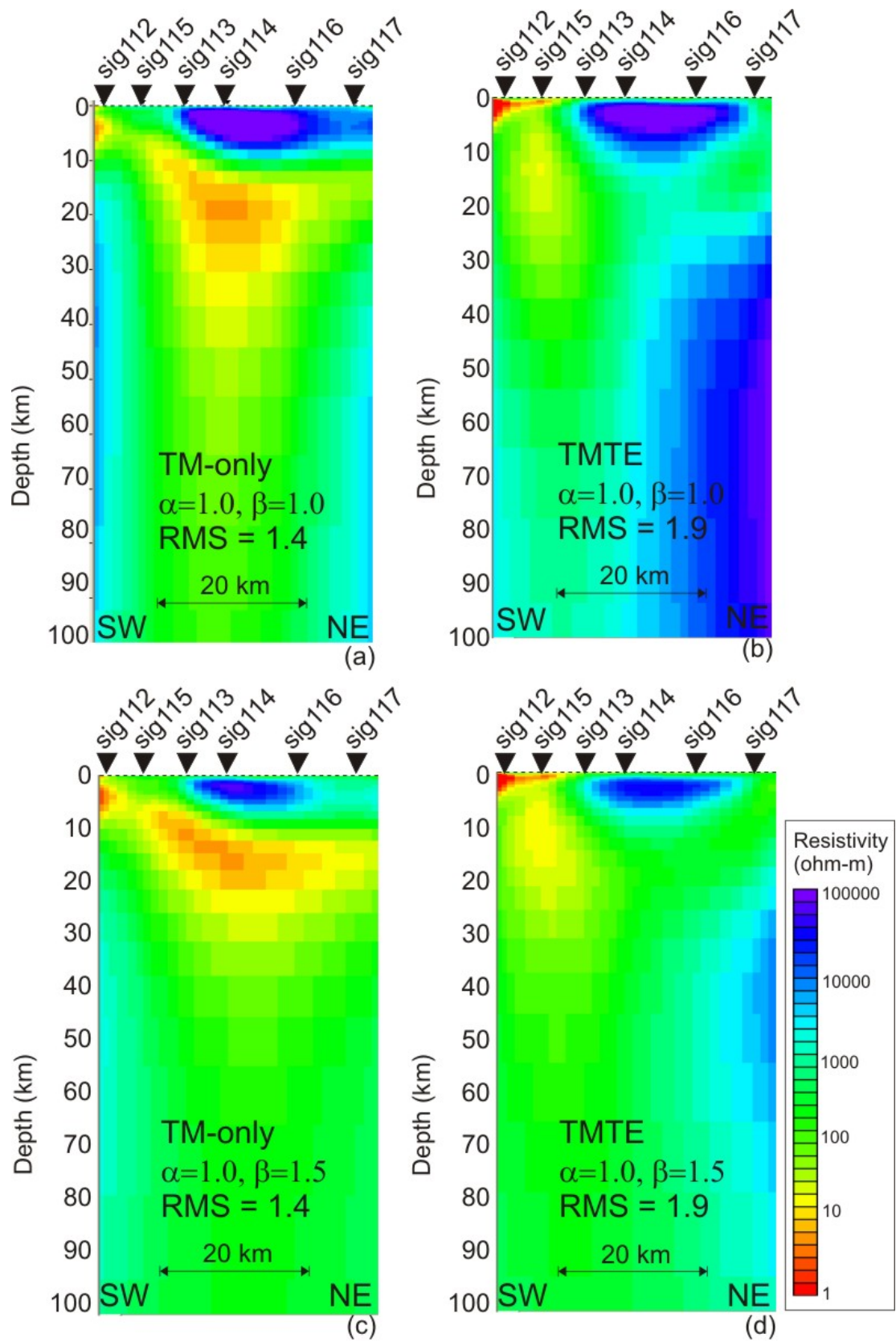


Figure 21

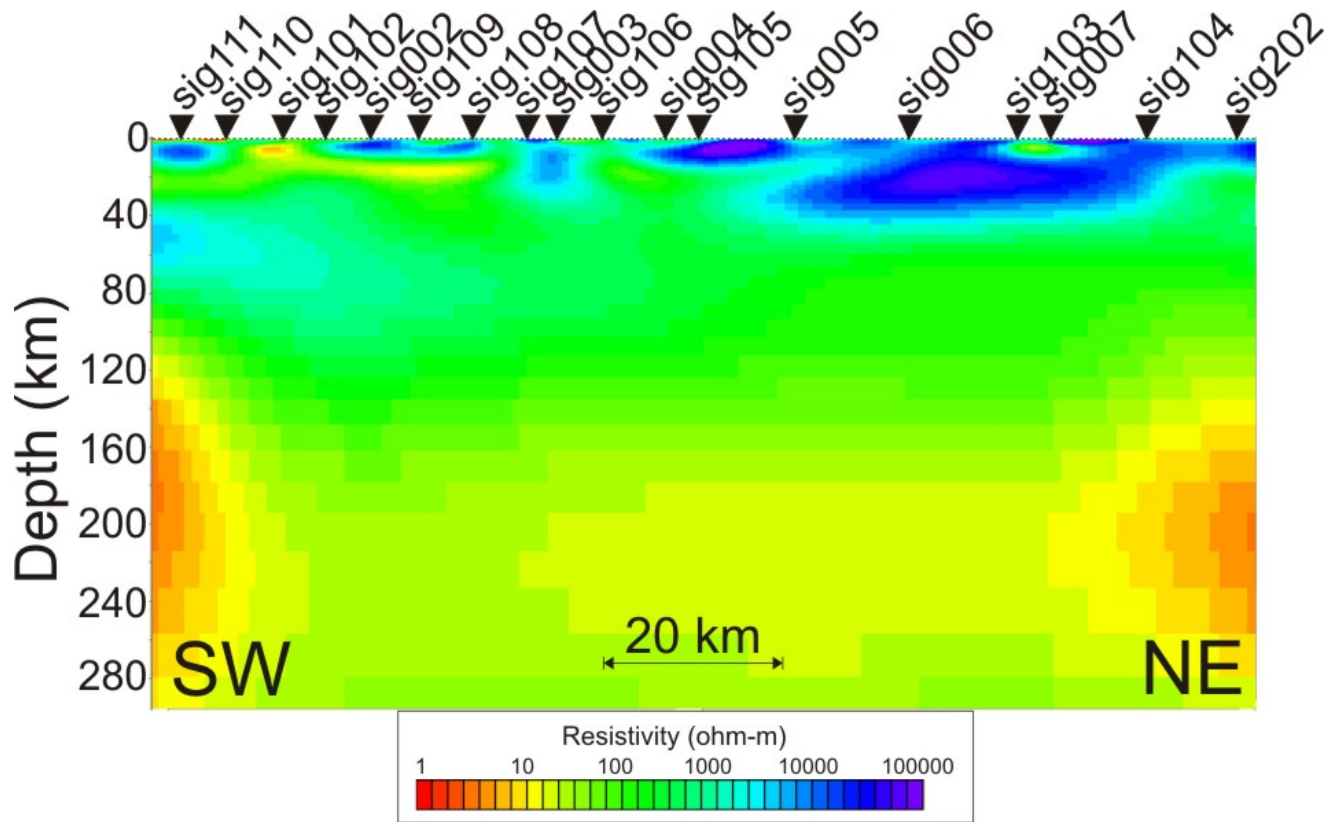


Figure 22